

Supplementary materials for

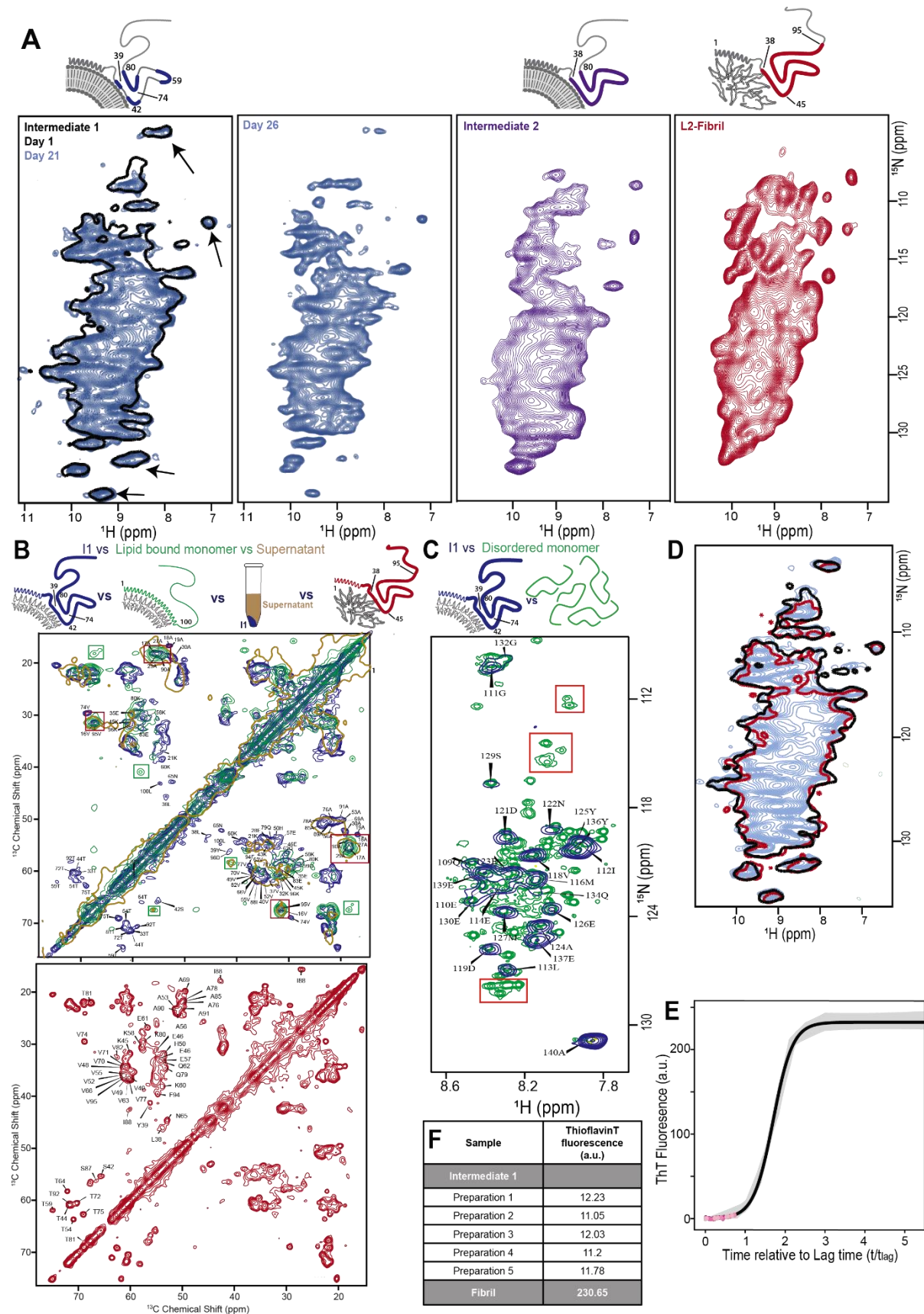
Lipidic folding pathway of α -Synuclein via a toxic oligomer

Vrinda Sant, Dirk Matthes, Hisham Mazal, Leif Antonschmidt, Franz Wieser, Kumar T. Movellan, Kai Xue, Evgeny Nimerovsky, Marianna Stampolaki, Magdeline Nathan, Dietmar Riedel, Stefan Becker, Vahid Sandoghdar, Bert L. de Groot*, Christian Griesinger*, Loren B. Andreas*

*Corresponding authors. Email: bgroot@mpinat.mpg.de, land@mpinat.mpg.de,
cigr@mpinat.mpg.de

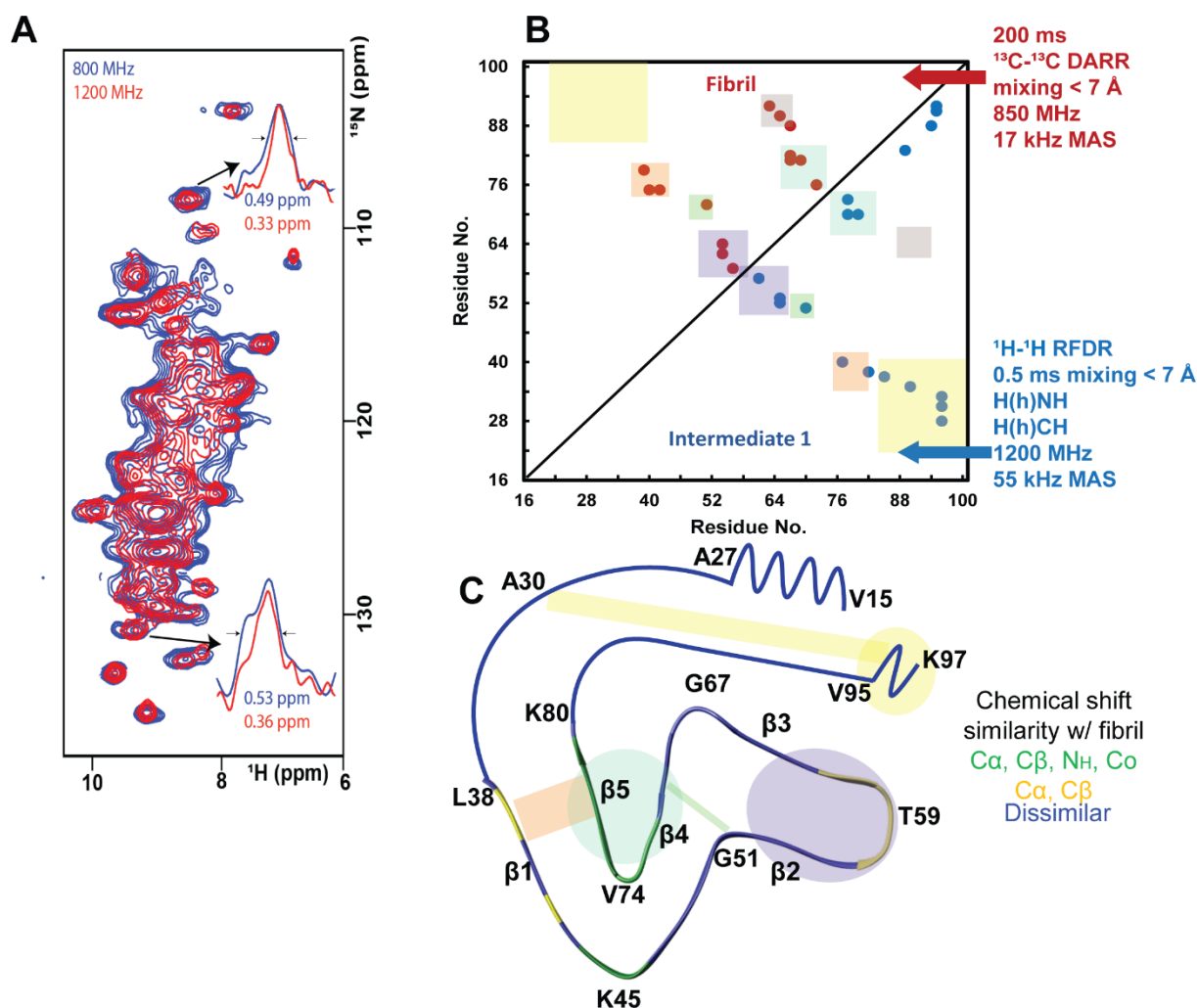
The file includes:

- Supplementary Figures 1 to 16
- Supplementary Note 1
- Tables S1 to S4
- Supplementary References

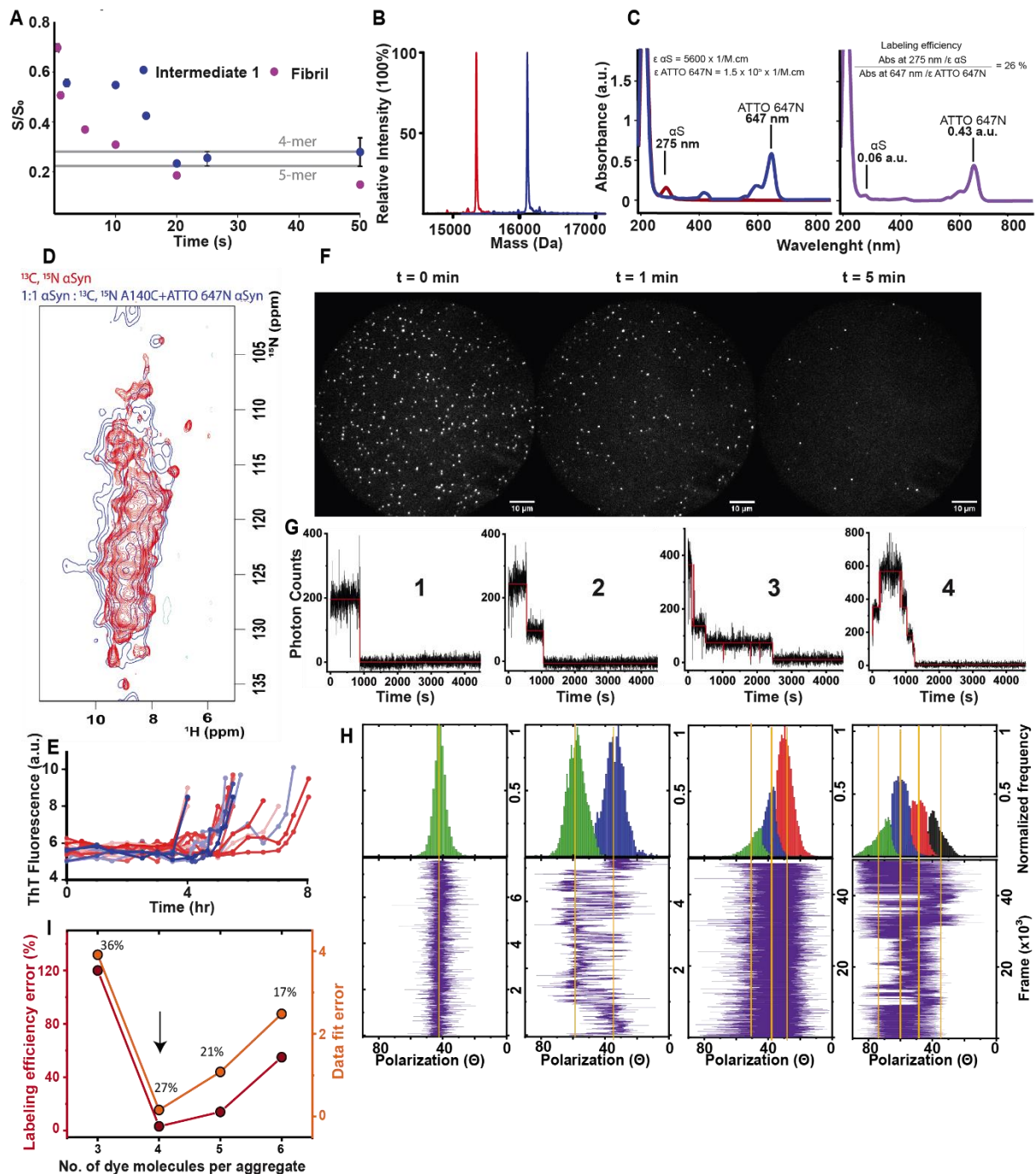


Supplementary Figure.1: The composition of an I1 sample and its stability. (A) Stability of Intermediate 1 (I1) during measurements: (H)NH spectrum of for ^{13}C , ^{15}N -labelled αS intermediate 1 at day 1 (black outline) and at day 21 (filled blue). During this time,

measurements were continuously acquired at an estimated sample temperature of 16°C. From left to right, progression from I1 to Intermediate 2 and the fibril can be seen as observed on ^{15}N -(H)NH fingerprint spectra. Arrows mark isolated resonances that broaden out when conversion begins. When the spectrum begins to look like the one at Day 26, measurements are stopped, and a new sample is prepared. **(B)** (*Top*) The I1 sample does not contain lipid bound monomers: ^{13}C - ^{13}C correlation spectrum with 20 ms DARR mixing for ^{13}C , ^{15}N labelled I1 (blue) and lipid bound monomer recorded at 850 MHz at 17 kHz MAS with sequence assignments. Resonances corresponding to V16, A17, V95, K96 and Q99 (red boxes) can be found in lipid bound monomer spectra in Antonschmidt et.al.¹ and Comellas et.al.² as well as the BMRB entry 6968 [<https://dx.doi.org/10.13018/BMR6968>] for micelle bound monomer. These resonances are also observed for the same residues in I1. However, unassigned resonances in green boxes for the lipid bound monomer spectrum are unique to the monomer and are not observed for I1 indicating that any lipid bound monomer in an I1 sample is likely below the noise threshold (average signal to noise ratio 13:1). The supernatant obtained after spinning down an I1 sample is lyophilized and rehydrated and packed into a 1.3mm rotor. The ^{13}C - ^{13}C correlation spectrum (light brown) obtained shows a primarily helical species that shares several resonances with the lipid bound monomer, suggesting that monomeric species are retained in the supernatant after isolating I1. (*bottom*) ^{13}C - ^{13}C correlation spectrum with 20 ms DARR mixing for ^{13}C , ^{15}N labelled L2-fibril reported in Antonschmidt et.al. 2021¹⁷. **(C)** Flexible and highly mobile monomers are depleted in I1 samples: MAS NMR INEPT-(H)NH spectrum acquired at 55 kHz MAS of I1 (blue) overlayed on the ^1H - ^{15}N HSQC of ^{15}N - αS monomer in solution at 25°C (green). I1 peaks are assigned based on comparison with free monomer in solution. Backbone assignments were done based on BMRB entries 16300, 16904, 18857. An MAS NMR INEPT-(H)NH is expected to show only highly mobile regions in the sample. Resonances that are expected for free disordered monomer (residues 1-100) are not visible in the I1 sample (salient resonances in red boxes), indicating that the sample is depleted of highly mobile monomer required for further aggregation. For I1, resonances can be assigned to residues 109-140, confirming a flexible C-terminus. Monomer is detected in the supernatant after ultracentrifugation. **(D)** Batch-to-batch reproducibility of I1 samples. Three different samples shown in red, black and blue at day 1 of measurement have remarkable similarity. **(E)** Aggregation kinetics reported by ThT fluorescence. A fit from four independent repeats is shown as a solid black line. The data were fitted as described in Antonschmidt et.al.¹⁷ using AmyloFit. The standard deviation from four samples is shown as the shaded gray area. The time axis is shown relative to the lag time, previously determined to be 6.6 ± 2.0 hours. Data points



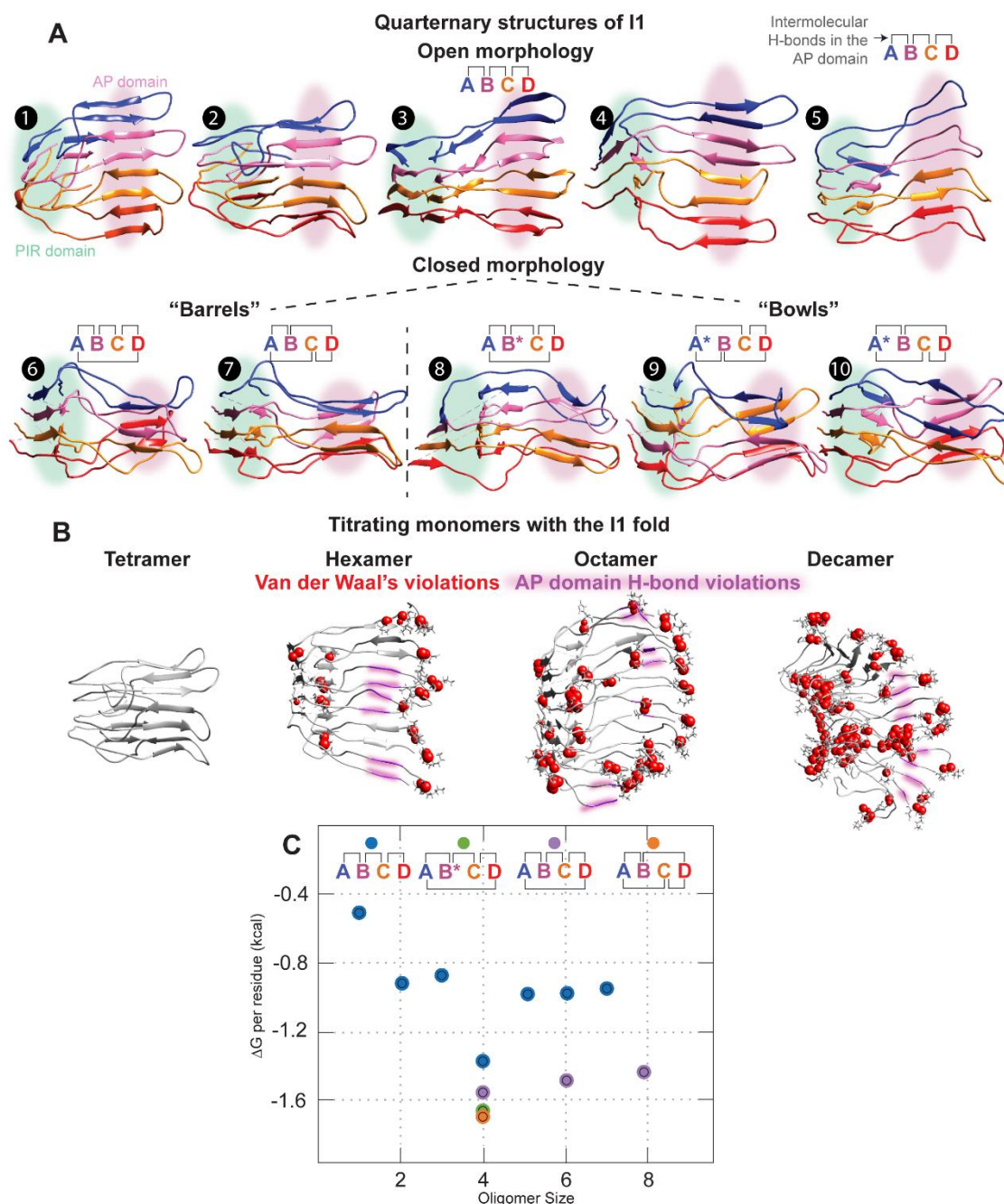
Supplementary Figure 3: Topology of I1. (A) Comparison of ^1H - ^{15}N correlation spectra measured at the 1200 MHz and 800 MHz spectrometers with 55kHz MAS showing dramatic improvement in homogenous linewidths. (B) Contact map comparing long range distances ($i \rightarrow n$ ($n \geq i \pm 4$)) measured for the fibril (^{13}C - ^{13}C contacts) and I1 (^1H - ^1H backbone contacts). I1 contacts were recorded with (H)NHH and (H)CHH spectra. (C) Contacts mapped onto the expected fold for I1. The chemical shift similarity with the fibril is shown on the fold. As shown in Fig.1D, I1 and the L2 fibril have similar helical residues between V16-T22. Note that cryo-electron microscopy of the L2 fibril shows a β -strand for V16-T22, suggesting that a fraction of the NMR sample likely contains β -strands³.



Supplementary Figure.4: Size determination of I1 by NMR and fluorescence spectroscopy. (A) CODEX curve for I1 (blue) and L2 fibril (pink) for a single ^{13}C isotopically labeled site at H50 $^{13}\text{C}\epsilon$ shows that the I1 curve plateaus at ~ 0.25 . Error bars are propagated from the root mean square of a noise region for each spectrum. The signal plateaus at the inverse of the number of spins over which magnetization can equilibrate and rate of decay informs about the distance between each spin. The L2 fibril curve did not fully plateau within the times used for magnetization to exchange and notably the curve decays faster suggesting a shorter distance between the isotopically labeled H50 $^{13}\text{C}\epsilon$ nuclei between each molecule in the L2 fibril. Source data are provided as a Source Data file. (B) Deconvoluted mass spectra of WT

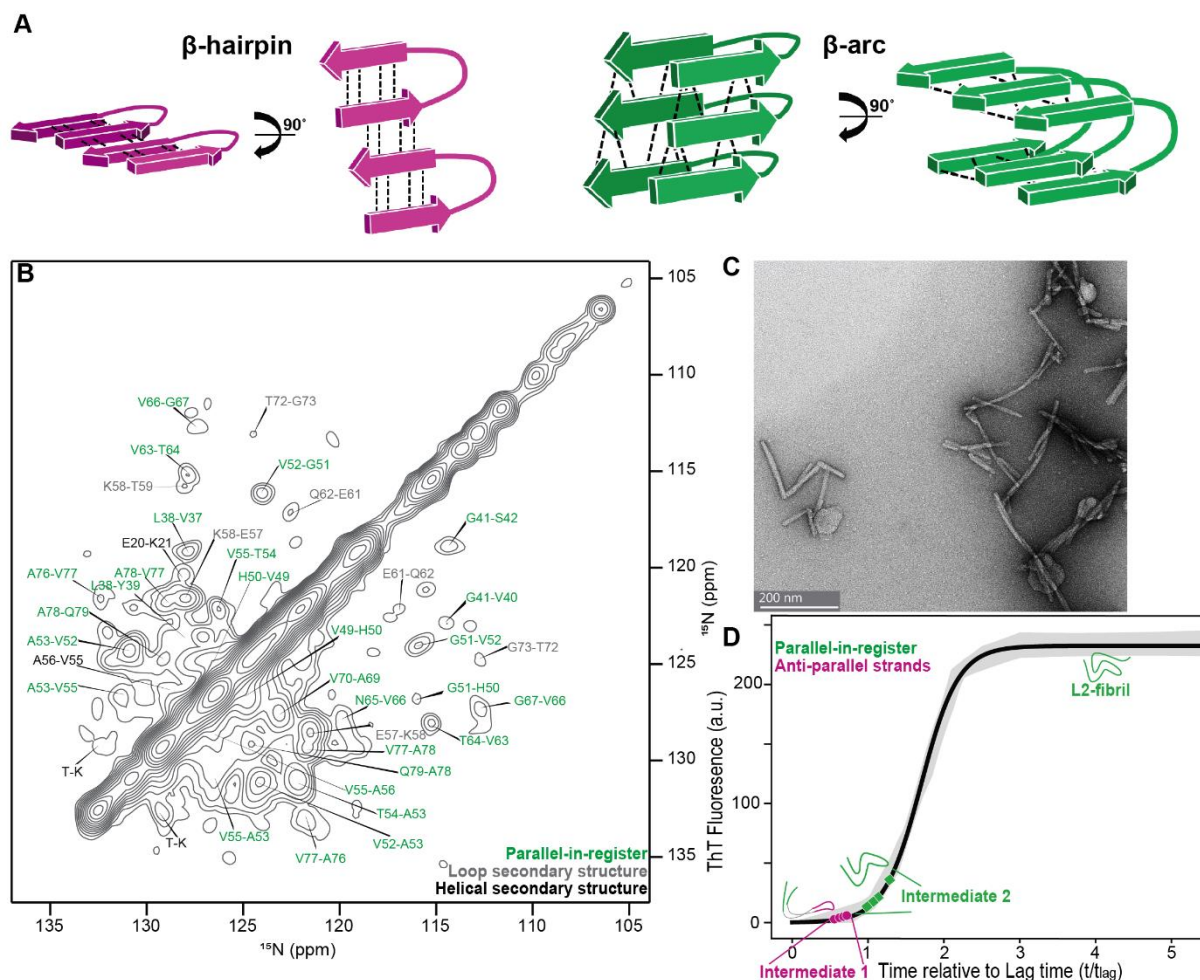
dye unlabeled α S (red) and A140C dye labeled α S (blue) showing proteins of mass 15351.72 ± 2.40 Da and 16121.42 ± 2.39 Da, respectively, confirming the dye tagging of the protein with approximately 100% yield. (C) Absorbance spectra of α S used to calculate labeling efficiency of the ATTO647N dye after mixing dye labeled protein stock with unlabeled stock. (*Left*) absorbance spectra of unlabeled α S shows a maximum at 275 nm. The extinction coefficient (ϵ) is stated on top and is based on tyrosine content⁴. Overlaid is the absorbance spectra of ATTO 647N in DMSO shows a maximum at 647 nm. ϵ stated on top is from the manufacturer. (*Right*) Absorbance spectra of about 75% unlabeled α S and 25% dye labeled α S shows a peak at 275 nm and 647 nm as expected. The concentrations are calculated according to the Beer-Lambert law using the given ϵ and a path length of 0.2 cm. The peak at 275 nm gives the concentration of the total protein ($\sim 54 \mu\text{M}$) and the peak at 647 nm gives the concentration of the dye labeled protein ($\sim 14 \mu\text{M}$), resulting in a labeling efficiency of $\sim 27\%$. (D) ^1H - ^{15}N correlation spectra comparison for 1:1 dye bound: wild type. I1 wild type (red) and dye bound I1 (blue) serve as a fingerprint that confirm that an I1 type fold is retained in the dye bound aggregate. (E) ThT aggregation curves of WT dye unlabeled α S (shades of red) and A140C dye labeled α S (shades of blue) show that the kinetics of dye labeled α S are within the variation presented by dye unlabeled α S. Source data are provided as a Source Data file. (F) Snapshots of single-molecule fluorescence images at different times of I1 labeled with ATTO647N (experimental labeling efficiency of 26%). The images show dispersed aggregates and most aggregates are completely photobleached in about 5 minutes upon continuous irradiation with a laser. (G) Selected intensity time traces which show clear 1, 2, 3 and 4 bleaching steps. Source data are provided as a Source Data file. Histogram of bleaching steps is depicted in Fig.2D. (H) Examples of polarization traces (purple) with 1, 2, 3 and 4 different polarization states (yellow lines) from super-resolved images in Fig.2E-H. The precision of each localization scales as the inverse square root of the number of photons, $\sigma_{loc} \sim \frac{1}{\sqrt{N}}$, which can vary for different fluorophores due to the heterogeneity in their photophysical properties. For demonstrated time traces the average localization precision is 0.34 nm, 0.52 nm, 0.38 nm and 0.25 nm for states 1, 2, 3 and 4, respectively. The normalized segmented histograms (green, blue, red and black) represent the relative population of each polarization state in the time trace. Source data are provided as a Source Data file. (I) A binomial distribution is used to fit bleaching step histograms. Varying the total number of monomers allows one to extract the theoretical labeling efficiency as a fit parameter. The labeling error (the difference between fitted labeling efficiency and experimental value) is plotted as a function of the number of monomers per oligomer (red curve), pointing to the tetramer as the best model (black arrow). In addition, the residual of each

fit, plotted as a function of the number of monomers per oligomer (orange curve), confirms that the tetramer model fits best to the experimental data. Source data are provided as a Source Data file.



Supplementary Figure.5: Conformers of I1 (G36-K80 segment) modeled with CYANA and all-atom restrained MD show that tetramer is the optimal size for I1. NMR restraints in Supplementary Table.1 are used to construct these conformers. (A) Conformers are numbered 1-10. Two morphological categories formed by an I1-type fold: Open and closed. All

conformers feature two domains: a fibril like PIR domain and AP domain, highlighted in green and pink, respectively. Structures are colored by chain and show the pattern of intermolecular H-bonds. Chain with missing intramolecular H-bonds is denoted by a star. Open conformers differ primarily on the tightness of loops at K45 and V74. Closed structures differ in the order of intermolecular H-bonds in the AP domain. The “bowl” type sub-category of closed structures have one strand that is missing intra-molecular H-bonds. Conformers were produced with CYANA (1,2,4,5,7,9,10) and all-atom restrained MD (3,6,8). (B) Titrating monomers with the open I1 fold shows steric (red spheres) and hydrogen bond (highlighted purple ribbons) violations arising for oligomers larger than tetramers. For larger oligomers, restraints are simply replicated for each molecule and the structure calculation is performed in CYANA. Chimera is used to identify Van der Waals violations larger than 0.6 Å. H-bond violations are considered when larger than 0.3 Å. Violations are depicted if they are found in more than 15 out of 20 structures. Terminal residues are not included in the analysis. Violations occurring in the AP domain can be seen as the aggregate gets larger. (C) Solvation free energy per residue calculations^{5,6} for different oligomer sizes shows that there is an energy minimum for the open and barrel morphology for the 4-mer. Different structures are denoted by chain IDs on top. Source data are provided as a Source Data file.



Supplementary Figure.6: Fibrillar intermediate 2 (I2) features a β -arc at V52-V66. (A) Schematic showing the distinct hydrogen bonding in a β -hairpin and β -arc. Hydrogen bonds are shown as dotted black lines. In a β -hairpin, characteristic of globular proteins, hydrogen bonding occurs between consecutive strands via backbone hydrogen bonds. In a β -arc, characteristic of amyloid fibrils, consecutive strands are held together by sidechain hydrophobic, or charge interactions. The backbone hydrogen bonds occur between consecutive molecules, leading to stacking of these molecules. **(B)** ^{15}N - ^{15}N correlation spectra showing exclusively next neighbor contacts characteristic of PIR β -sheets. The I2 preparation was identified based on its characteristic (H)NH spectrum (Fig.S1A). The resonances were assigned based on chemical shift similarity to the L2 fibril and helical termini were assigned based on chemical shift similarity to I1. **(C)** TEM image of an I2 sample shows short filamentous strands representative of fibrillar intermediates. **(D)** Aggregation kinetics are observed with ThT fluorescence. The ThT values at which different samples of I1 and I2 have been isolated are shown in pink and green, respectively. I1 is primarily present in the lag phase of aggregation, whereas I2 in the growth phase. The aggregation curve is reproduced from Fig.S1E. Note that for each intermediate ThT values are shown only at the time when aggregation was stopped and samples were isolated.

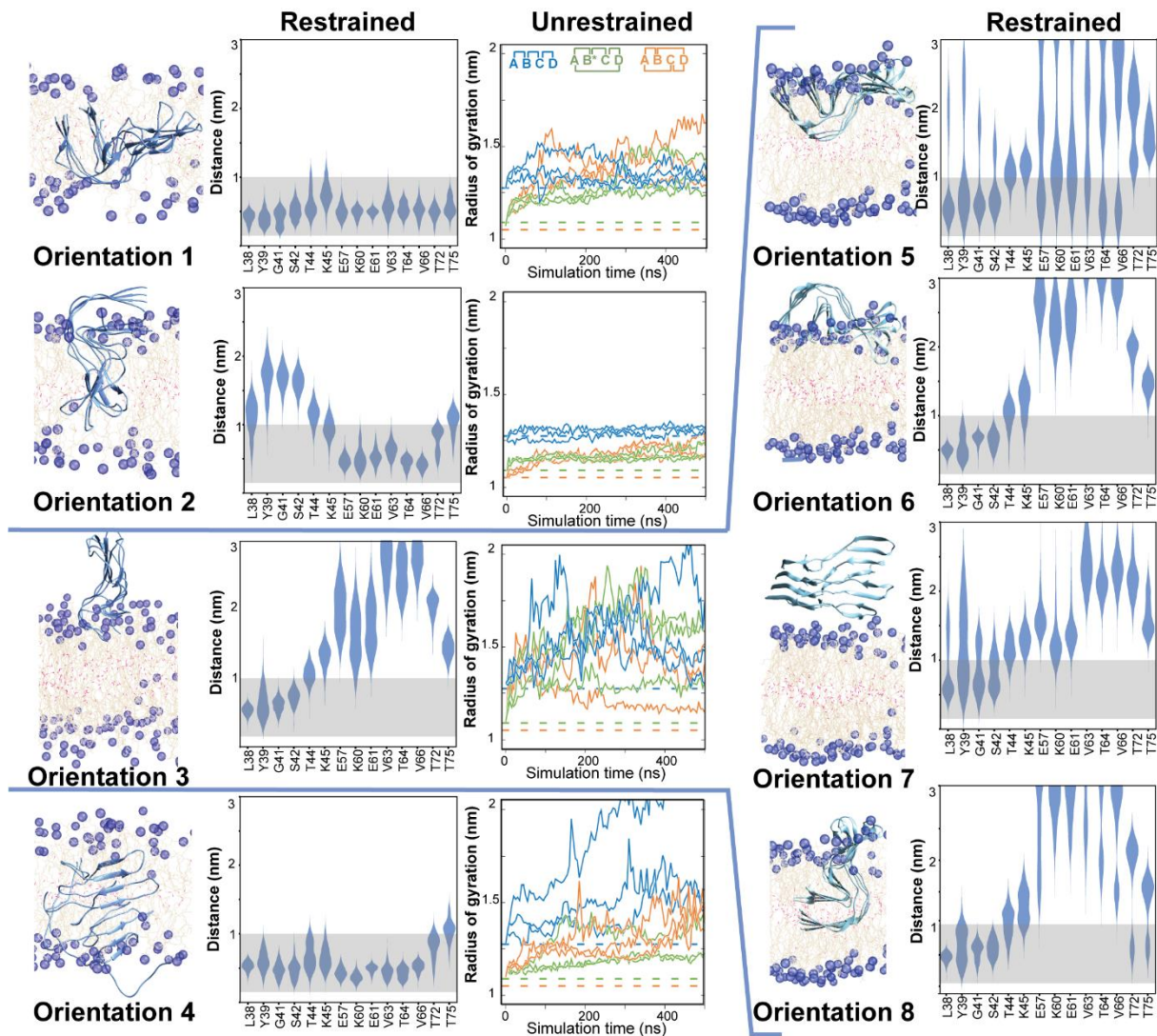
Supplementary Note 1

All-atom Molecular Dynamic (MD) simulations were performed in two steps to probe placement of I1 in lipid bilayers. First, a short segment of I1 (G36-T81), consisting of the four β -strands was simulated with restrained MD simulations in a total of eight different orientations on a POPC and POPA (molar ratio 1:1) lipid bilayer (Supplementary Table.3). This was followed by unrestrained MD simulations to evaluate dynamics and agreement with experimental distance restraints for orientations 1 to 4 (Fig.S8). Fig.S8 provides an overview of all simulations performed to select orientations 1 and 2 as candidates fulfilling the lipid-protein contacts and concludes that orientation 3 and those similar to it, where the AP domain is outside the bilayer, do not reproduce lipid-protein contacts. One conformer from each type of AP domain morphology (open, closed: bowl and barrel) was probed in the unrestrained simulations for orientation 1 to 4 and only the open and bowl morphologies were carried over to the next step because they showed most stable structures. In the next step, a longer segment consisting of helices and β -strands (V16-Q99) was simulated with unrestrained MD simulations. Fig.S9 shows detailed analysis of structural data that are used to assess consistency with experimentally observed parameters for the V16-Q99 segment of I1 in orientations 1, 2 and 3, in particular the agreement with experimental lipid contacts. The open and bowl morphologies in orientation 1 and 2 continue to agree with experimental lipid contacts as well as H-bonds in the AP domain.

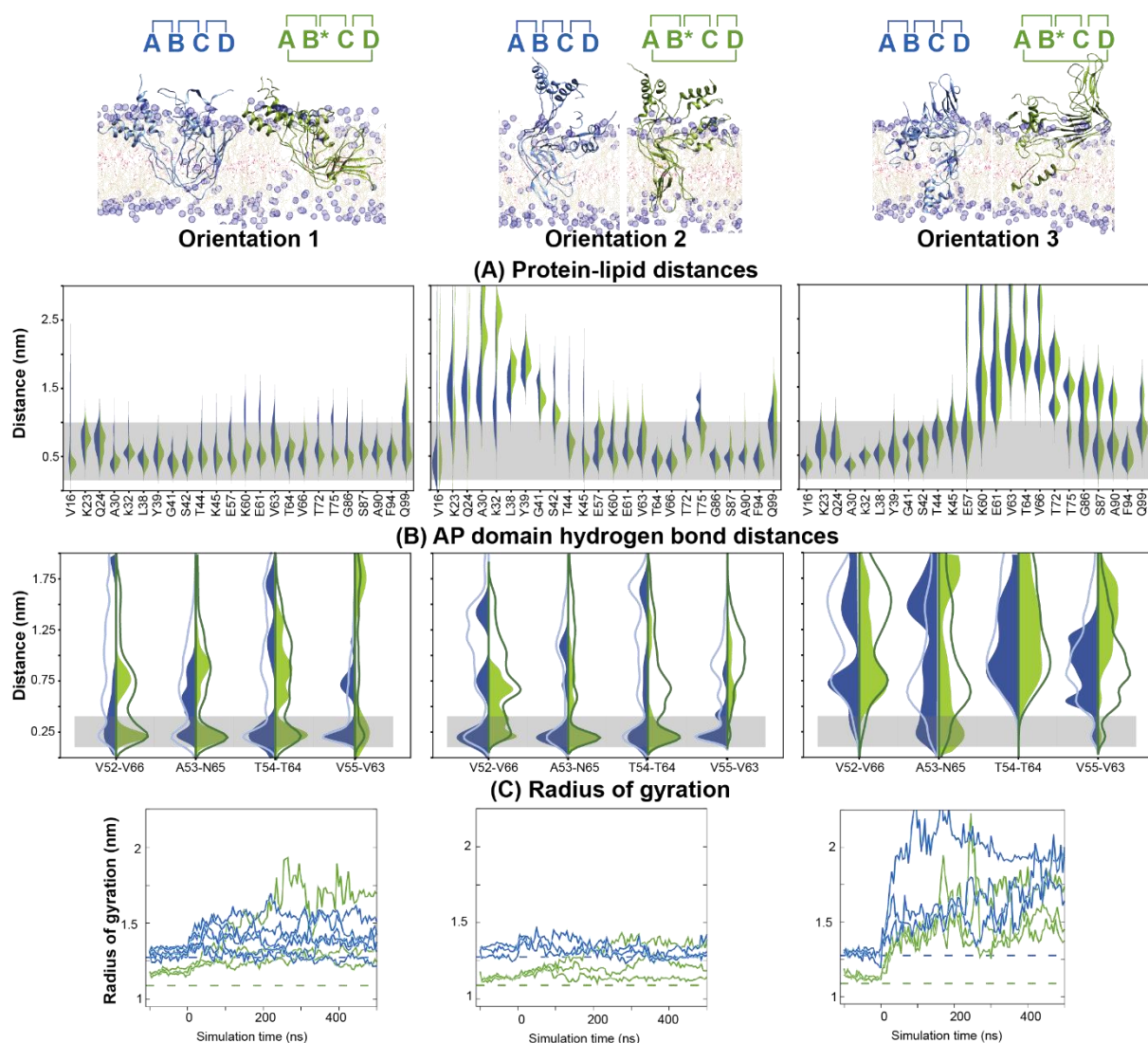
An I1 sample thus is likely to contain an ensemble of open and bowl morphologies in orientations 1 and 2.

In the next step, MD simulations were used to probe the ability and extent of I1 in orientation 1 and 2 to permeabilize lipid bilayers at two different salt concentrations (A: 150mM NaCl; B: 100mM NaCl and 40mM CaCl_2). These simulations were initiated from I1 models with refined N- to C-, and C-terminal structure restraints (Supplementary Table.4).

Fig.S10 shows detailed analysis of structural data that are used to evaluate and compare with experimentally observed parameters for the V16-Q99 segment of I1 in orientations 1 and 2.



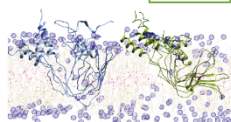
Supplementary Figure 8: Overview of initial testing which identifies orientations 1 and 2 as best candidates. To probe the orientations of I1 with respect to a bilayer, a construct (G36-T81) without the helices was used and the AP domain was restrained. Distances between lipid and protein protons during the last 250 ns of each trajectory were followed. The lipid contacts observed are under the ‘restrained’ column and the gray bar shows the experimental range for the lipid contacts. Here orientations 1-4 are stably bound to the bilayer whereas orientations 5-8 convert from their initial orientation (as seen in the snapshots) to the state in orientation 3 i.e. showing now close contacts to the bilayer. In this case, the AP domain hydrogen bonds behave as in orientation 3. Unrestrained simulations were performed with three morphologies (open: blue, bowl: green, barrel: orange) for orientations 1-4. Radius of gyration (backbone atoms of H50-G67) shows the AP domain dynamics compared to the initial structure (broken lines). In orientation 3 and 4, the radius of gyration shows a dynamic and expanding AP domain for all three probed morphologies. In all four cases, the barrel AP domain morphology shows dynamic structures and was not used for further analysis. Source data are provided as a Source Data MD file.



Supplementary Figure 9: MD simulations of α S I1 show that lipids are important to stabilize the AP domain. A construct V16-Q99 is simulated with two morphologies (open: blue, bowl: green). For each orientation, snapshots from the simulation are shown where purple represents headgroup choline, tan the lipid acyl chains and pink, the terminal methyl. Panels A-D quantify parameters from simulations for orientations 1, 2, and 3 (left to right). Gray region in each panel shows the distance range expected from experiments and depends on the concentration of protons in the sample, mixing time and type of measurement. (A) Distances observed in the simulation between backbone amide protons and lipid protons. (B) H^N -O distances corresponding to hydrogen bonds in the AP domain. Blue and green lines show statistics accumulated from 6 simulations for orientation 1 and 3 simulations for orientations 2 and 3. Filled distributions represent statistics from the simulation that agreed best with experimental parameters. H-bond distances belonging to the same atom pair from all four different molecules were pooled together. The long H-bond distances can be attributed to the transient formation of edge strands, like in the open morphology, that have dangling inter-molecular H-bonds and the transient loss of intra-molecular H-bonds, like in the bowl morphology. Since the simulations are unrestrained, spontaneous sampling and exchange between morphologies can be observed. Simulations are considered to agree with experiment when a significant frequency can be observed within the gray range. (C) Radius of gyration (backbone atoms of H50-G67) for each scenario shows the AP domain dynamics compared to the initial structure (broken lines). Open morphology (blue traces) is rather stable in orientations

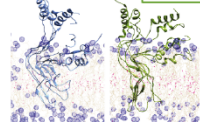
1 and 2, The bowl morphology (green traces) is more dynamic in orientation 1 compared to orientation 2. In orientation 3, both morphologies are very dynamic. Despite this, the bowl in orientation 1, satisfies H-bonds and lipid contacts for the majority of the time. Putting together the analysis of all parameters, we see that the open and bowl morphologies agree with a large fraction of experimental protein-lipid contacts and hydrogen bonds in orientations 1 and 2. In comparison to orientations 1 and 2, in orientation 3, the residues in the AP domain spend most of the time outside the bilayer. In this case, the AP domain is solvent exposed and unfolds. Fewer H-bonds are observed within the gray range and dynamics in the AP domain are observed for orientation 3. Source data are provided as a Source Data MD file.

(A) **ABCD** **AB*CD**



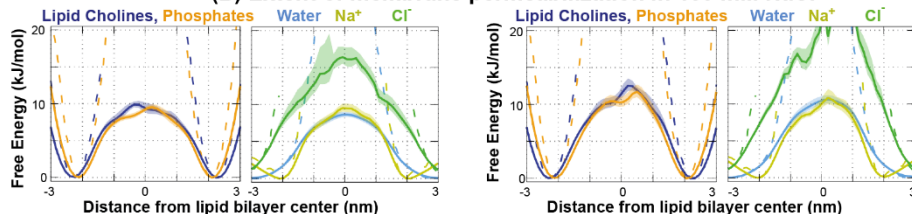
Orientation 1

ABCD **AB*CD**

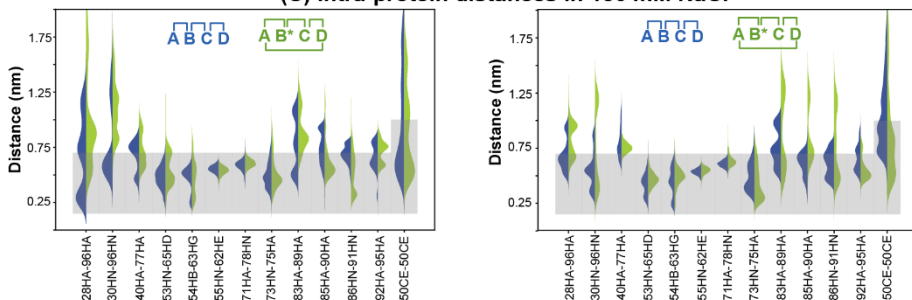


Orientation 2

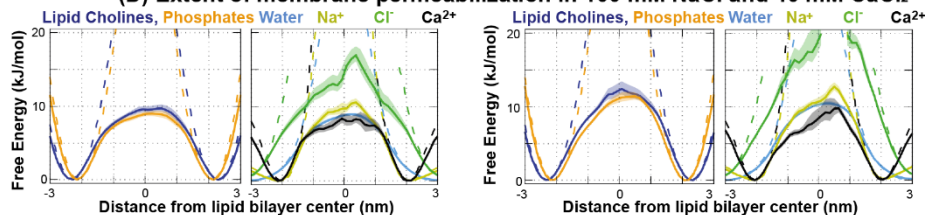
(B) Extent of membrane permeabilization in 150 mM NaCl



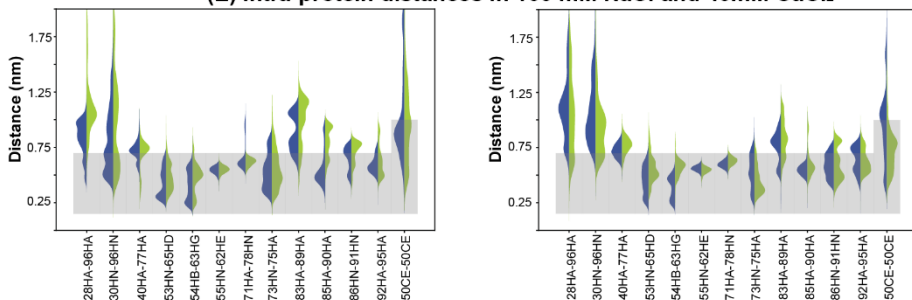
(C) Intra-protein distances in 150 mM NaCl



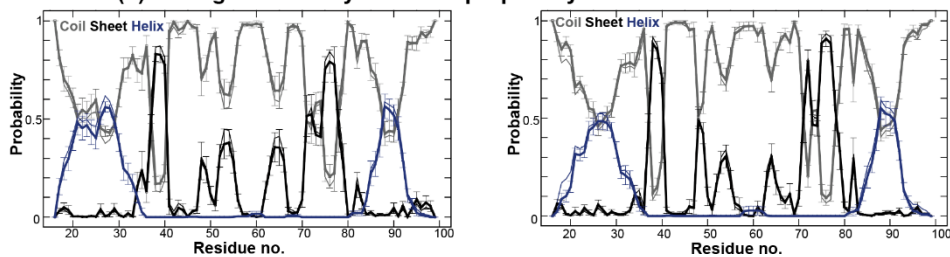
(D) Extent of membrane permeabilization in 100 mM NaCl and 40 mM CaCl₂



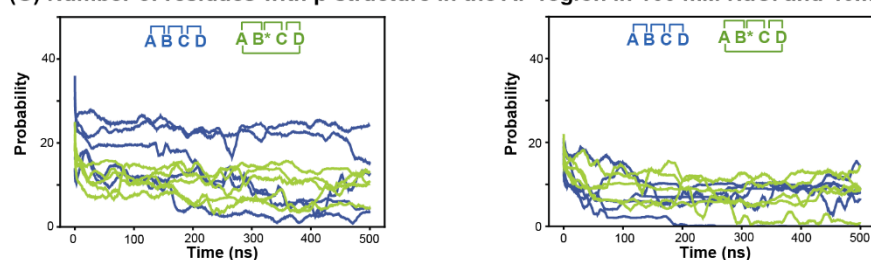
(E) Intra-protein distances in 100 mM NaCl and 40mM CaCl₂



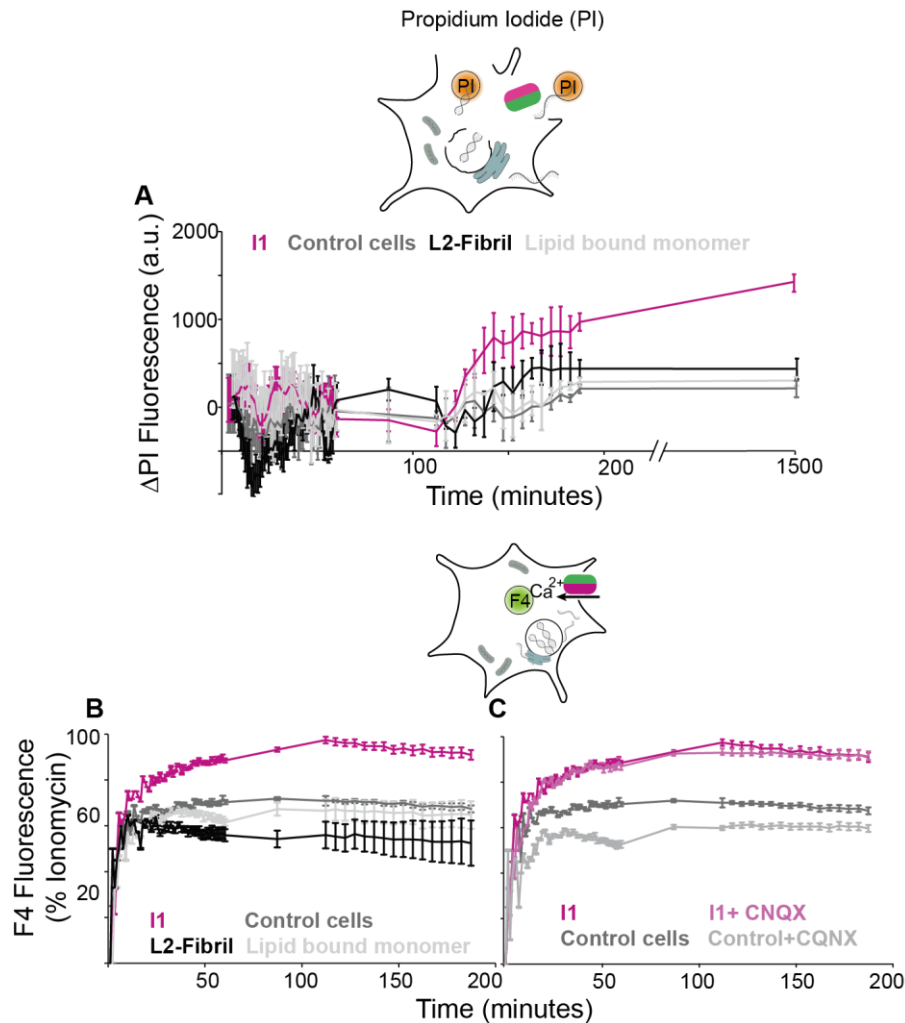
(F) Average secondary structure propensity in 100 mM NaCl and 40mM CaCl₂



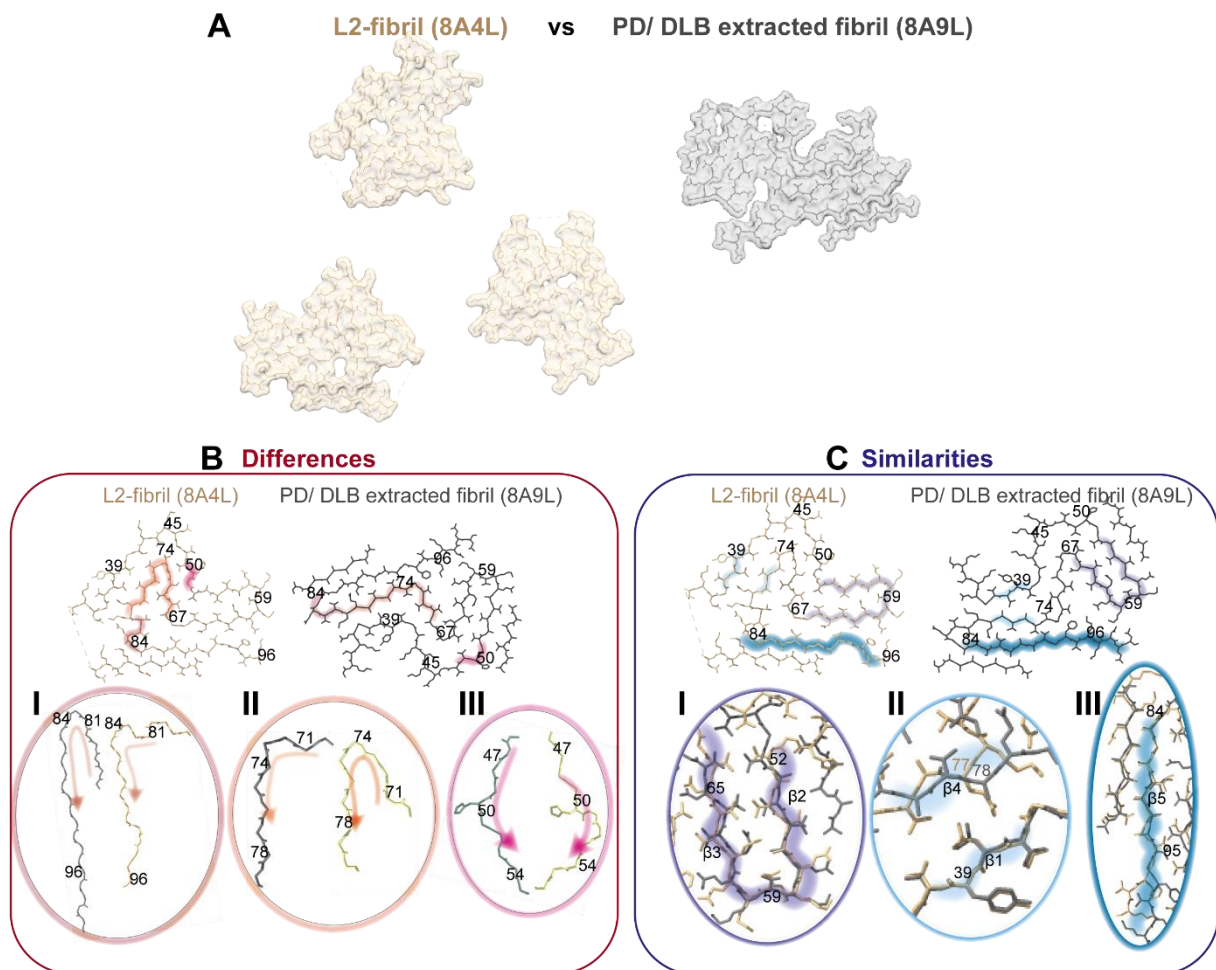
(G) Number of residues with β -structure in the AP region in 100 mM NaCl and 40mM CaCl₂



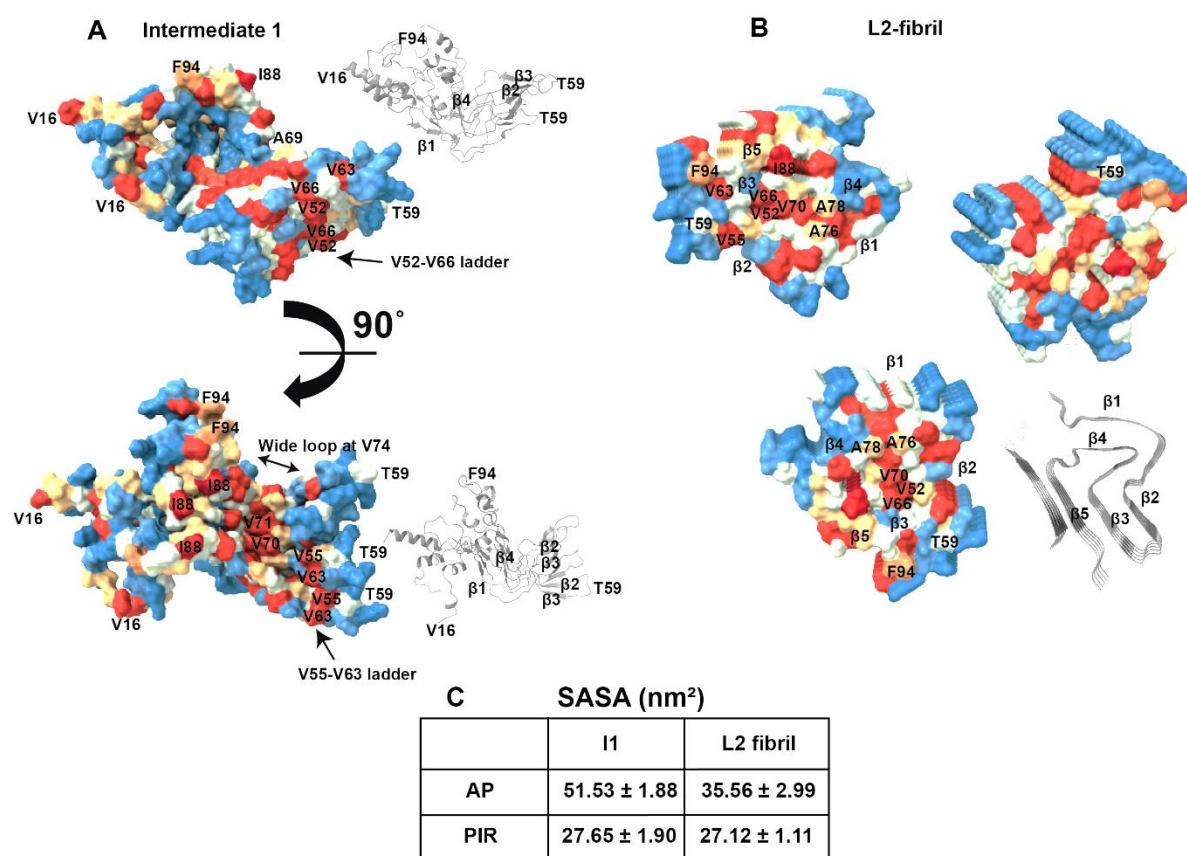
Supplementary Figure.10: I1 causes membrane defects in MD simulations. Bilayers equilibrated with I1 models in orientation 1 and 2 show a reduced energy barrier for permeation of lipid headgroups, water and cations across the membrane center compared to an unperturbed bilayer without bound I1. **(A)** Illustrations of orientations 1 (left) and 2 (right). The derived properties in panels B-G are presented respectively for these orientations. **(B)** Extent of membrane disruption observed in MD simulations for I1 (150mM NaCl) in orientation 1 (left) and orientation 2 (right). The density based free energy profiles across a bilayer for lipid choline (purple), phosphates (orange), water (blue), Na^+ (yellow), Cl^- (green). Dotted lines show the free energy profiles for unperturbed bilayers. **(C)** Intra-protein distances for open (blue) and bowl (green) morphology as observed during the simulation for orientation 1 (left) and orientation 2 (right). Gray region shows the distance range expected from experiments. **(D)** Extent of membrane disruption observed in MD simulations for I1 (100mM NaCl and 40 mM CaCl_2) orientation 1 (left) and orientation 2 (right). The density profiles across a bilayer for lipid choline (violet), phosphates (orange), water (blue), Na^+ (yellow), Cl^- (green) and Ca^{2+} (black). Dotted lines show the density profiles for unperturbed bilayers. **(E)** Intra-protein distances for open (blue) and bowl (green) morphology as observed during the simulation for orientation 1 (left) and orientation 2 (right). Gray region shows the distance range expected from experiments. **(F)** Average secondary structure propensity for I1 models in orientation 1 (left) and orientation 2 (right). **(G)** Time course of β -structure propensity for open (blue) and bowl (green) morphologies in the AP domain. The change in secondary structure in the first tens of ns is due to the removal of distance restraints used during the equilibration of the membrane inserted oligomers prior to the production runs (data not shown in the plot). After this initial phase, no significant changes in the β -structure content of the AP domain were found over time and across all probed simulation systems. Source data are provided as a Source Data MD file.



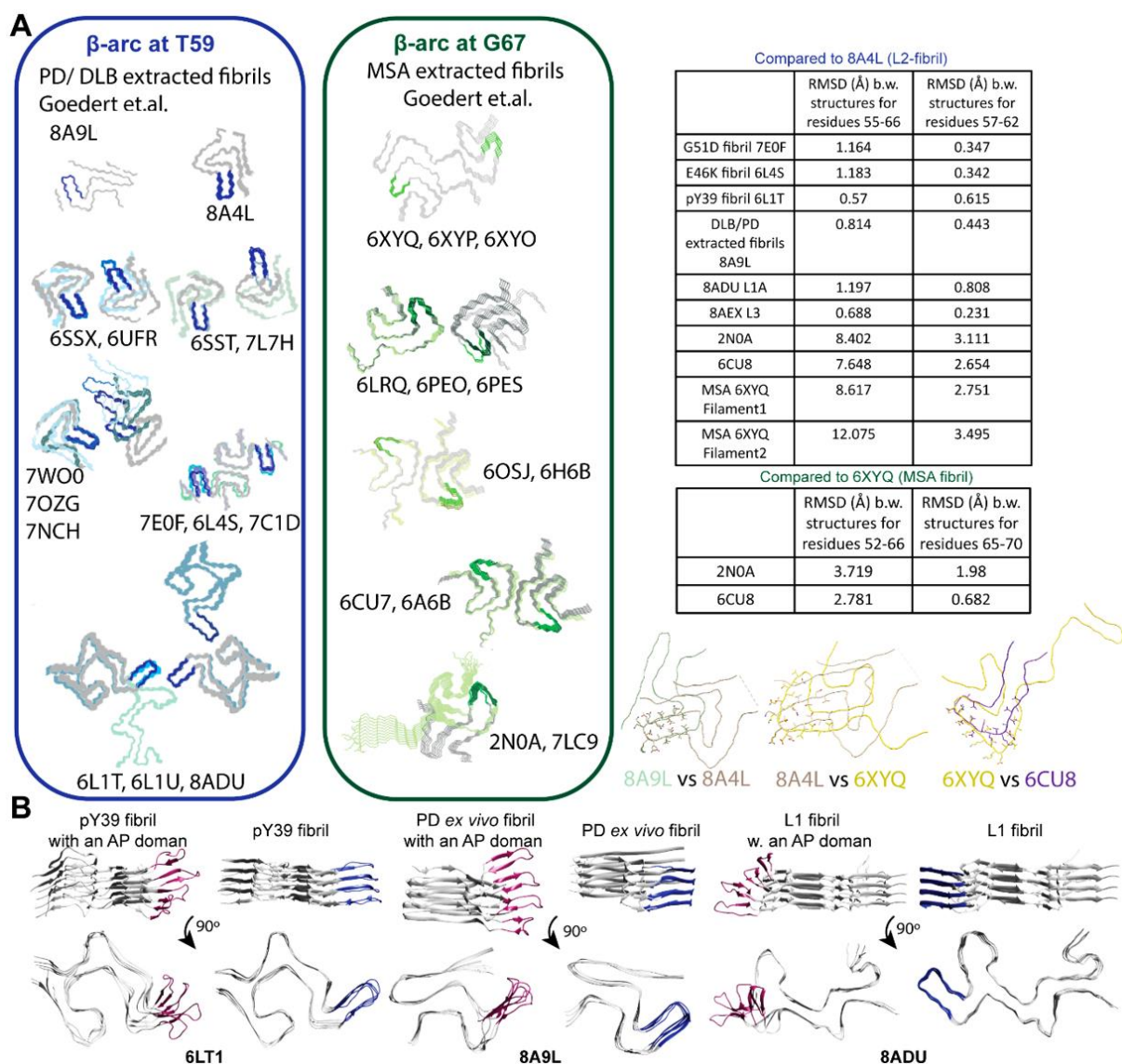
Supplementary Figure.11: I1 disrupts membranes. (A) Propidium iodide (PI) fluorescence shows that cell death begins at ~120 minutes for cells incubated with I1, whereas the Ca^{2+} influx starts to increase at ~15 minutes after incubation. PI is a cell membrane impermeable dye that fluoresces when it binds nucleic acids. Due to its impermeable nature, this happens only when the membrane ruptures as illustrated in the schematic on top. (B) Calcium influx is measured by fluorescence of Fluo-4 (F4) loaded in SH-SY5Y cells as in Fig.4F. The I1 (pink) and control cells (dark gray) curves are reproduced from Fig.4E. Monomers (light gray) and fibrils (black) do not show a significant difference from the control. (C) The Ca^{2+} influx caused by I1 is not related to the action of AMPAR (AMPA glutamate receptor) as inhibiting AMPAR with CNQX (cyanquixaline) does not change the Ca^{2+} uptake curves for I1. Error bars represent standard error of the mean in panels for 6 replicates from two different preparations (A-C). I1 curves in panels (B) and (C) are reproduced from Fig.4F. The concentration of α S in I1, L2-fibril and lipid bound monomer samples was 0.6 μ M and the lipid concentration in each sample was estimated to be 60 μ M, 3 μ M and 60 μ M respectively. The CNQX concentration was 5 μ M. Source data are provided as a Source Data file.



Supplementary Figure.12: Comparison of L2 fibril with the Lewy fold extracted from PD/DLB brains. (A) The L2 fibril features three proto-filaments while the PD/DLB fibrils always occur as single filaments. (B) Differences between the folds of individual protofilaments of the two fibrils occur at (I) the turn at G84 which is 180° in the PD/DLB fibril and 90° in the L2 fibril, (II) the at G73 which is 90° in the PD/DLB fibril and $\sim 160^\circ$ in the L2 fibril and (III) the bend at H50-G51 which is concave in the PD/DLB fibril and convex in the L2 fibril. (C) Differences between the folds of individual protofilaments of the two fibrils include (I) the β -arc at T59, (II) the interaction between $\beta 1$ and $\beta 4$ and the structure of the $\beta 5$ strand.

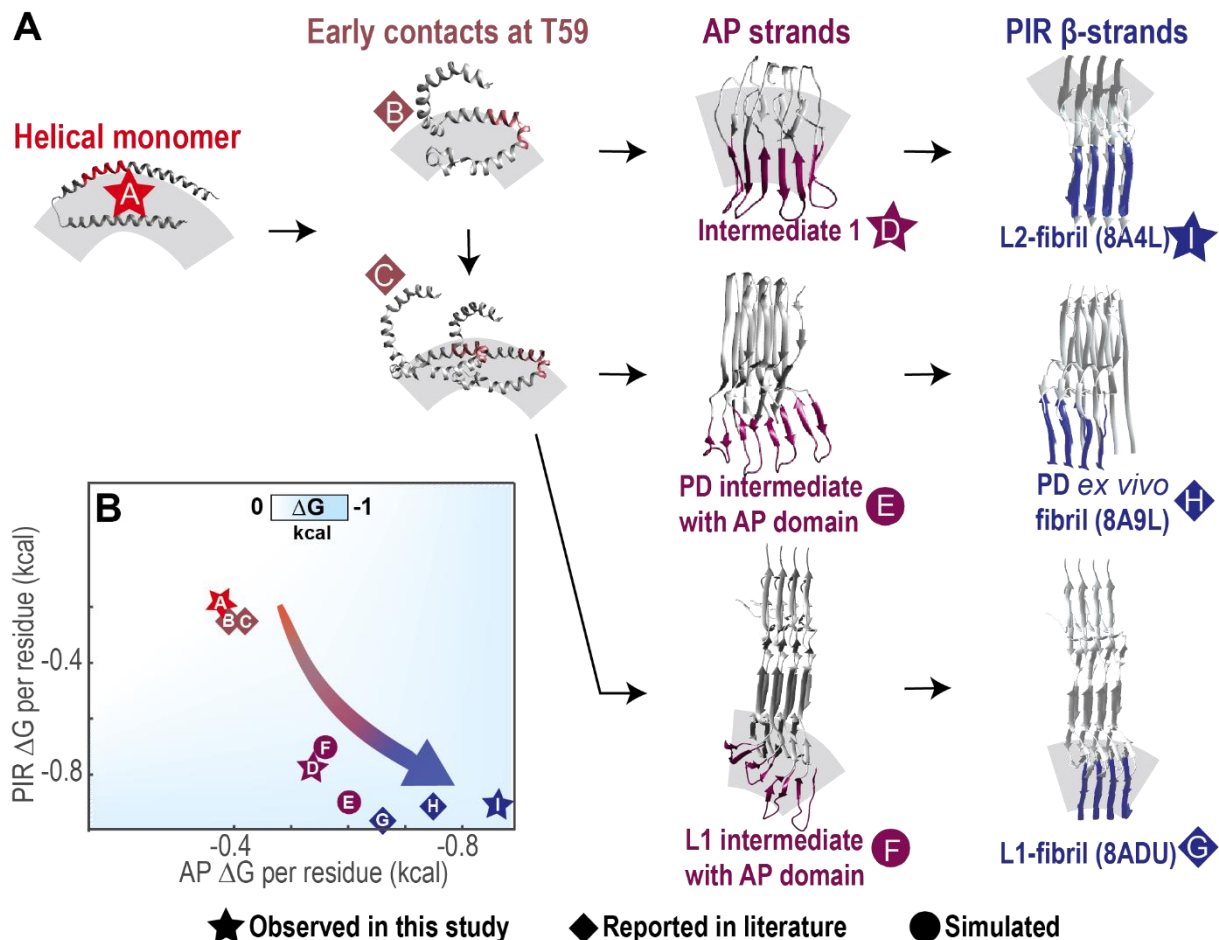


Supplementary Figure.13: Kyte-Doolittle hydrophobicity⁸⁵ surface of I1 (A) and L2-fibril (B). (A) Blue-white-red shows increasing hydrophobicity. In I1, AP β -strands ($\beta 1$ and $\beta 2$), have two exposed surfaces with ladders built by hydrophobic residues V52, V66 and V55, V66. Additionally, the loop at V74 is wider in I1 compared to the L2-fibril. (B) In the fibril, V52-V66 get buried in the hydrophobic core of the fibril, along with V71. The V74 loop gets tighter, preventing the exposure of V71 and A69 to the solvent. The hydrophobic residues F94 and I88 only get buried in the hydrophobic core of the fibril, when $\beta 5$ folds in on $\beta 3$. (C) The hydrophobic solvent accessible surface area (SASA) for the AP domain (residue 50-67) and in the PIR domain (residue 37-44 and 75-80) based on MD simulations of tetrameric models with I1- (G36-T81) and L2-fold (G36-K97). Averages (and standard deviations) were calculated for the 50 ns of three 100 ns long simulations each.



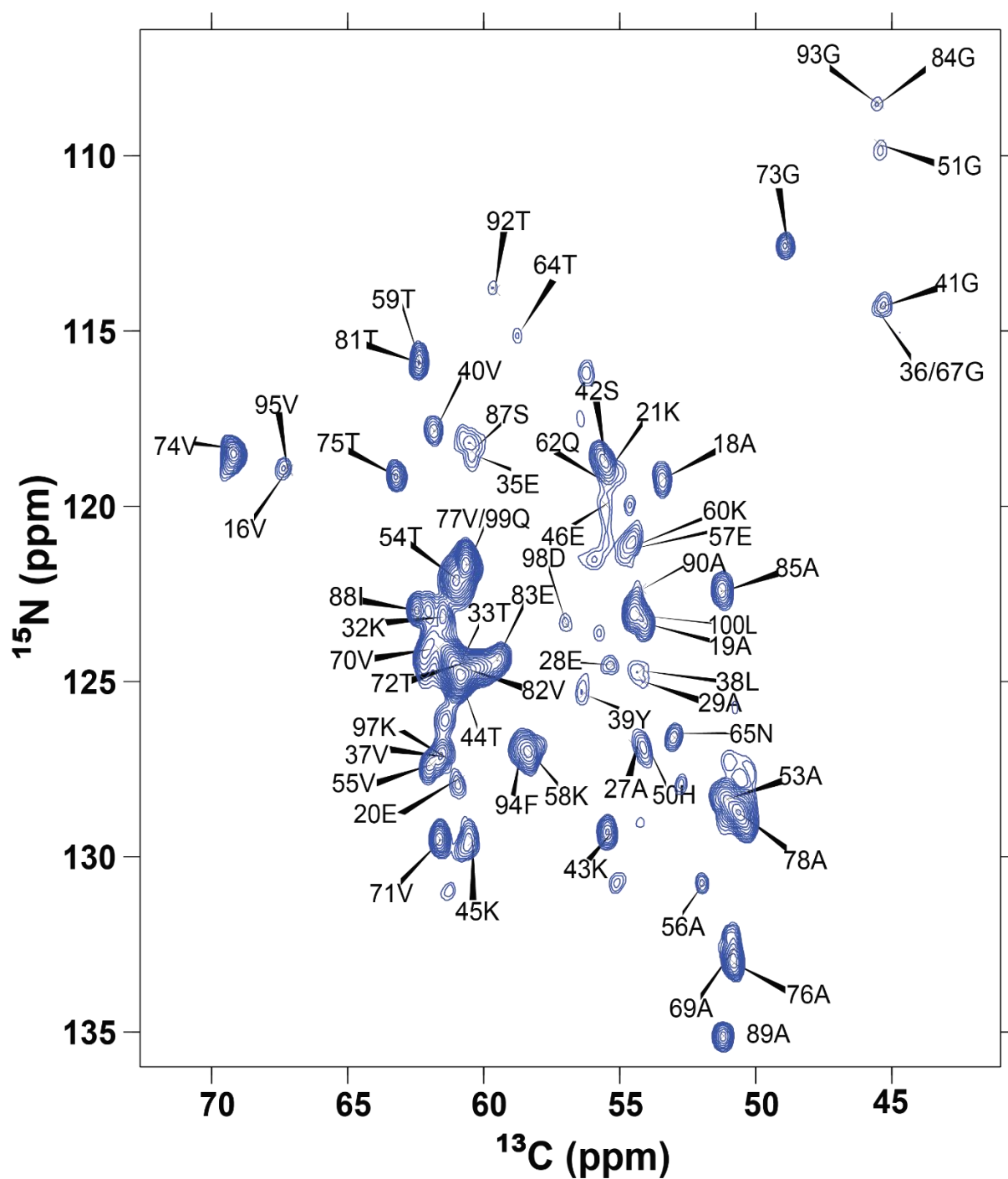
Supplementary Figure.14: Classification of αS fibrils and their respective intermediates.

(A) A classification can be made of αS fibrils based on the morphology of the hairpin turn at T59. A β-arc at T59, as found in the L2 fibril type, is conserved in a large set of αS fibril polymorphs (blue), including extracted fibrils from Parkinson's and Lewy Body Dementia patients (8A9L), pY39 recombinant fibril (6L1T), L1 and L3 lipidic polymorphs, E46K (6UFR, 6L4S) and G51D (7E0F) fibrils. By contrast, all other αS fibril polymorphs, like the MSA-fold (6XYQ), has the same type of β-arc at G67 instead (green). This is despite some of these fibrils having a distinct topological fold, for example, Greek-key versus Triple-L. The same distinction has previously been made by Sawaya and Eisenberg et.al. (Cell, 2021)⁵ who referred to the β-arc at G67 fibrils as “boot-type” and the β-arc at T59 fibrils as “sandal-type.” (B) Snapshots from MD simulations showing different tetrameric oligomers modelled from fibril polymorphs with a β-arc at T59 (blue strands) can accommodate anti-parallel β-strands (pink strands) at this position.



Supplementary Figure.15: Proposed aggregation cascade for α S-fibril polymorphs with a β -arc at T59. (A) Schematic showing transition from the helical α S monomer to PIR fibrils with a β -arc at T59. The residues (V52-V66) that transition from β -hairpin to β -arc are shown with red in the helical state, with light pink when a bend at T59 is introduced, with dark pink when they are structured as AP β -strands and blue in the PIR state. Letters enclosed in a shape represent each structure. The shape determines if the structure was observed in this study (star), observed in literature (diamond) or simulated with all-atom MD (circle). β -hairpins/ AP strands represent an intermediate folding state. The species observed on-pathway to the L2 fibril is referred to as “intermediate 1 (I1).” Intermediates which we propose would have an AP domain like I1 but the rest of the structure is more like their respective fibrils’ folds are referred to as “L1 intermediate with AP domain” and “PD intermediate with AP domain”. (B) Solvation free energy per residue calculations^{5,6} for the PIR (y-axis) and AP(x-axis) domains show how an α S molecule is stabilized during the folding of the L2 fibril, L1-fibril, and PD *ex vivo* fibril. The solvation energy does not consider the additional stabilization provided by lipids in lipidic aggregates. Rather, it is an estimate of the intrinsic properties of the structure that contribute to its energetic stability in an aqueous environment. Source data are provided as a Source Data file. **Not only can the structures of L1 and PD *ex vivo* fibrils accommodate AP domains at T59, but the formation of these domains is energetically favorable.** **Helical monomer (Structure A):** α S starts as a lipid bound helical monomer in the preparation used in this work¹ with relatively high energies for the PIR and AP residues. **Early contacts at T59 (Structures B, C):** A monomer and dimer have been observed that are bent at T59 when bound to lipids⁷, which appears to stabilize PIR and AP domains to a small extent. **β -hairpin at T59 (Structures D-F):** To minimize energy in both segments, the PIR residues adopt a fibril like structure, and intra- and inter- molecular H-bond formation is completed in the AP domain in four copies of

α S. This is observed in I1 and simulated in the L1 and PD *ex vivo* fibril structures. **β -arc at T59 (Structures G-I):** Finally, additional stabilization is provided to both, the PIR and AP segments, by the transition to a β -arc at T59. This transition appears to relieve strain in the PIR region due to twist induced by AP strands, reducing the energy per residue for V37-S42 and T75-K80. The β -arc at T59 packs more hydrophobic residues in the fibril core than the AP-strand arrangement, drastically reducing the solvation energy for V52-V66. The relative stability of the fibrils depends on the distinct arrangements of the PIR domains.



Supplementary Figure 16: Assigned spectra of the structured segments of I1. 2D $\text{C}\alpha\text{-N}$ projection from a 3D (H)CANH spectrum with specific resonance assignments. Continuous assignments were obtained for stretches 16-22, 27-32, 34-68 and 69-100, resulting in 64% sequence coverage of what is considered the structured core of αS (residues 1-100).

Supplementary Table.1: Contacts used for CYANA and MD structure calculation

Residues	Restraint	Upper Limit (Å)	Lower Limit (Å)
37-43, 76-80	Nearest-neighbor intermolecular H-bonds between backbone N/H and O of residue i with backbone O and N/H of residues i-1 and i+1, respectively	O-N 3 Å, O-H 2.8 Å	O-N 2.7 Å, O-H 1.8 Å
63 O- 55 N/H, 63 N/H- 55 O	Intra-molecular anti-parallel H-bonds	O-N 3 Å, O-H 2.8 Å	O-N 2.7 Å, O-H 1.8 Å
65 O- 53 N/H, 65 N/H- 53 O	Intra-molecular anti-parallel H-bonds	O-N 3 Å, O-H 2.8 Å	O-N 2.7 Å, O-H 1.8 Å
66 O- 52 N/H, 66 N/H-52 O	Inter-molecular anti-parallel H-bonds	O-N 3 Å, O-H 2.8 Å	O-N 2.7 Å, O-H 1.8 Å
54 O- 64 N/H, 54 N/H-64 O	Inter-molecular anti-parallel H-bonds	O-N 3 Å, O-H 2.8 Å	O-N 2.7 Å, O-H 1.8 Å
	On account of chemical shift similarity w. L2 fibril		
	76 C β - 71 C γ	7	
	44 C γ – 74 C γ	4	
	47 C α – 74 C γ	5	
	77 C γ - 38 C δ	7	
	Observed in (H)NHH and (H)CHH spectra		
	65 H δ - 53 H	7	
	62 H ϵ - 55 H	7	
	54 H β – 63 H γ	7	
	71 H α -78 H	7.5	
	73 H- 75 H α	7	
	40 H α - 77 H α	7	
	28 H α - 96 H α	7	
	30 H $_N$ - 96 H $_N$	7	
	Observed in (H)N(H)(H)NH spectra at 3.46 ms mixing		
	H $_N$ - H $_N$ contacts between A89-T92, G86-K97, V82-T92, G86-I88, T81- S87, K97- V95	4	

Supplementary Table.2: Acquisition parameters for NMR measurements

Spectrum	Transfer	Nucleus	rf (kHz)	time CP (ms)	Ramp	t1 (ms)	t2 (ms)	t3 (ms)	SW3 (ppm)	SW2 (ppm)	SW1 (ppm)	No. of scans	Time (hr)	Temperature Set (K)	Probes/Magnet	Recycle delay (s)	MAS (kHz)
hNH	1H-15N	1H	105	0.9	80-100 (1H)	20	42.5	-	30	-	36	32	3.5	235	1.3mm/800 MHz	1.6	55
		15N	38														
	15N-1H	1H	98	0.55	100-80 (1H)												
		15N	38														
hCaNH	1H-13C	1H	105	1.9	80-100 (1H)	15	6	18.8	34	36	36	8	56				
		13C	41														
	13C-15N	13C	26	13	63-94 (15N)												
		15N	37														
hCaNH	15N-1H	1H	98	0.35	100-80 (1H)												
		15N	38														
hCoNH	1H-13C	1H	106	4	80-100 (1H)	15	12.8	21.2	30	12	36	8	24				
		13C	41														
	13C-15N	13C	25	10	63-94 (15N)												
		15N	37														
hCoNH	15N-1H	1H	98	0.35	100-80 (1H)												
		15N	38														
hCoCoaNH	1H-13C	1H	106	4	80-100 (1H)	15	6	18.8	34	36	36	8	150				
		13C	41														
	13C-15N	13C	25	10	63-94 (15N)												
		15N	37														
hCoCoaNH	15N-1H	1H	98	0.35	100-80 (1H)												
		15N	38														
hCoCaNH	1H-13C	1H	106	4	80-100 (1H)	15	15.3	21.2	30	12	36	8	216				
		13C	41														
	13C-15N	13C	26	15	63-94 (15N)												
		15N	37														
hCoCaNH	15N-1H	1H	98	0.35	100-80 (1H)												
		15N	38														
hCaCbcaNH	1H-13C	1H	105	1.9	80-100 (1H)	15	5	18.8	34	74	36	4	405				
		13C	41														
	13C-15N	13C	26	15	63-94 (15N)												
		15N	37														
hCaCbcaNH	15N-1H	1H	98	0.33	100-80 (1H)												
		15N	38														
hNH	1H-15N	1H	105	0.9	80-100 (1H)	15	3	42.5	30	14	35	8	240				
		15N	38														
	15N-1H	1H	98	0.55													
		15N	38		100-80 (1H)												
hNH	13C 90°		63														
	1H 90°		111														
13C-13C DARR	1H-13C	1H	82	1.5		8.1	8.6	-	230	275	-	8	99	265	3.2mm/850 MHz	1.8	17
		13C	46														
		DARR (ms)	20														
hNHhNH	1H-15N	1H	105	0.95	80-100 (1H)	9	9	21	38	38	40	16	192	238	1.3 mm/1200 MHz	0.6	55.555
		15N	33														
	15N-1H	1H	100	0.5	100-80 (1H)												
		15N	33														

Supplementary Table.3: Overview of MD simulation systems and setup for runs with distance restraints.

System	Total no. simulations	Box dimensions	Total no. of atoms	Total no. of water molecules	Salt	Lipid composition	Figure(s)
8a4l w/o morph (G36-K97)	3 x L2 fibril AP morphology	10.7 x 10.7 x 7.6 nm	87993	28089	150 mM NaCl	n/a	S13
8a4l to I1 morph (G36-T81)	3 x open; 3 x bowl; 3 x barrel AP morphology	10.7 x 10.7 x 7.6 nm	89113	28768	150 mM NaCl	n/a	S13, S14
8a4l to I1 morph (V16-Q99)	2 x open; 2 x bowl AP morphology	12.6 x 12.6 x 8.9 nm	143404	46108	150 mM NaCl	n/a	S12
8a4l to I1 morph with additional structure restraints (V16-Q99)	3 x open; 3 x bowl AP morphology	12.6 x 12.6 x 8.9 nm	143404	46108	150 mM NaCl	n/a	
8adu to I1 morph (M1-Q99)	1 x open AP morphology	13.9 x 13.9 x 9.8 nm	192612	62172	150 mM NaCl	n/a	S13
8a9l to I1 morph (G31-L100)	1 x open AP morphology	11.3 x 11.3 x 7.9 nm	102291	32675	150 mM NaCl	n/a	S13
6l1t to I1 morph (M1-Q99)	1 x open AP morphology	13.0 x 13.0 x 9.2 nm	157839	50601	150 mM NaCl	n/a	S13
I1 Orientation 1 (G36-T81)	3 x open AP morphology	8.5 x 8.2 x 9.2 nm	64594	13634	150 mM NaCl	POPC: 79; POPA: 88	S8
I1 Orientation 2 (G36-T81)	3 x open AP morphology	8.6 x 8.3 x 9.2 nm	67702	13281	150 mM NaCl	POPC: 97; POPA: 103	S8
I1 Orientation 3 (G36-T81)	3 x open AP morphology	8.9 x 8.5 x 8.9 nm	69823	12716	150 mM NaCl	POPC: 115; POPA: 115	S8
I1 Orientation 4 (G36-T81)	3 x open AP morphology	8.5 x 8.2 x 9.1 nm	65846	13638	150 mM NaCl	POPC: 89; POPA: 85	S8
I1 Orientation 5 (G36-T81)	3 x open AP morphology	8.8 x 8.4 x 8.9 nm	68397	13256	150 mM NaCl	POPC: 105; POPA: 101	S8
I1 Orientation 6 (G36-T81)	3 x open AP morphology	8.7 x 8.4 x 9.1 nm	68576	12942	150 mM NaCl	POPC: 105; POPA: 110	S8
I1 Orientation 7 (G36-T81)	3 x open AP morphology	8.7 x 8.4 x 9.4 nm	70505	12525	150 mM NaCl	POPC: 120; POPA: 120	S8
I1 Orientation 8 (G36-T81)	3 x open AP morphology	8.8 x 8.5 x 8.8 nm	68036	13325	150 mM NaCl	POPC: 102; POPA: 99	S8

Supplementary Table.4: Overview of MD simulation systems and setup for runs with distance restraints.

System	Total no. simulations	Box dimensions	Total no. of atoms	Total no. of water molecules	Salt	Lipid composition	Figure(s)
I1 Orientation 1 (G36-T81)	3 x open; 3 x bowl; 3 x barrel AP morphology	8.5 x 8.2 x 9.2 nm	64594	13634	150 mM NaCl	POPC: 79; POPA: 88	S8
I1 Orientation 2 (G36-T81)	3 x open; 3 x bowl; 3 x barrel AP morphology	8.6 x 8.3 x 9.2 nm	67702	13281	150 mM NaCl	POPC: 97; POPA: 103	S8
I1 Orientation 3 (G36-T81)	3 x open; 3 x bowl; 3 x barrel AP morphology	8.9 x 8.5 x 8.9 nm	69823	12716	150 mM NaCl	POPC: 115; POPA: 115	S8
I1 Orientation 4 (G36-T81)	3 x open; 3 x bowl; 3 x barrel AP morphology	8.5 x 8.2 x 9.1 nm	65846	13638	150 mM NaCl	POPC: 89; POPA: 85	S8
I1 Orientation 1 (V16-Q99)	6 x open; 3 x bowl; 3 x barrel AP morphology	13.8 x 13.3 x 12.8 nm	227726	54971	150 mM NaCl	POPC: 230; POPA: 229	4, S9
I1 Orientation 2 (V16-Q99)	3 x open; 3 x bowl; 3 x barrel AP morphology	13.2 x 12.7 x 13.4 nm	230169	54614	150 mM NaCl	POPC: 244; POPA: 243	4, S9
I1 Orientation 3 (V16-Q99)	3 x open; 3 x bowl; 3 x barrel AP morphology	13.2 x 12.7 x 13.3 nm	230202	54335	150 mM NaCl	POPC: 247; POPA: 247	S9
I1 Orientation 1 with additional structure restraints (V16-Q99)	3 x open; 3 x bowl AP morphology	13.9 x 13.4 x 12.4 nm	217544	51736	150 mM NaCl	POPC: 229; POPA: 226	S10, S11
I1 Orientation 2 with additional structure restraints (V16-Q99)	3 x open; 3 x bowl AP morphology	13.9 x 13.4 x 12.4 nm	220622	51234	150 mM NaCl	POPC: 244; POPA: 248	S10, S11
I1 Orientation 1 with additional structure restraints (V16-Q99)	5 x open; 5 x bowl AP morphology	13.9 x 13.4 x 12.4 nm	217490	51709	100 mM NaCl, 40 mM CaCl ₂	POPC: 229; POPA: 226	S10, S11
I1 Orientation 2 with additional structure restraints (V16-Q99)	5 x open; 5 x bowl AP morphology	13.9 x 13.4 x 12.4 nm	220568	51207	100 mM NaCl, 40 mM CaCl ₂	POPC: 244; POPA: 248	S10, S11

References for Supplementary Information

1. Antonschmidt, L. *et al.* Insights into the molecular mechanism of amyloid filament formation: Segmental folding of α -synuclein on lipid membranes. *Sci Adv* 7, eabg2174 (2021).
2. Comellas, G., Lemkau, L. R., Zhou, D. H., George, J. M. & Rienstra, C. M. Structural intermediates during α -synuclein fibrillogenesis on phospholipid vesicles. *J Am Chem Soc* 134, 5090–5099 (2012).
3. Frieg, B. *et al.* The 3D structure of lipidic fibrils of α -synuclein. *Nature Communications* 2022 13:1 13, 1–10 (2022).
4. Weinreb, P. H., Zhen, W., Poon, A. W., Conway, K. A. & Lansbury, P. T. NACP, A Protein Implicated in Alzheimer's Disease and Learning, Is Natively Unfolded. *Biochemistry* 35, 13709–13715 (1996).
5. Sawaya, M. R., Hughes, M. P., Rodriguez, J. A., Riek, R. & Eisenberg, D. S. The expanding amyloid family: Structure, stability, function, and pathogenesis. *Cell* 184, 4857–4873 (2021).
6. Eisenberg, D. & McLachlan, A. D. Solvation energy in protein folding and binding. *Nature* 319, 199–203 (1986).
7. Schwarz, T. C. *et al.* High-resolution structural information of membrane-bound α -synuclein provides insight into the MoA of the anti-Parkinson drug UCB0599. *Proc Natl Acad Sci U S A* 120, e2201910120 (2023).

Description of Additional Supplementary Files

File Name: Supplementary Movie 1

Description: Transition from β -hairpin to β -arc. A trajectory is mapped between an I1 conformer and the L2-fibril. The AP domain residues V52-V66 are highlighted in pink when they form a β -hairpin, as in I1. The H-bonds between the two strands in the AP domain are slowly seen breaking as the segment transitions to an L2-fibril type β -arc which is represented in blue. The video plays from the β -arc back to the β -hairpin with a 90° rotation.

File Name: Supplementary Movie 2

Description: Snapshots from the unrestrained MD simulation of the I1 open morphology in orientation 1 in the bilayer. In this orientation, the PIR and AP domains are in the same leaflet of the lipid bilayer. Pink ribbons represent the AP domain, green ribbons the PIR domain. Blue spheres represent the POPC headgroup nitrogen and a surface map of lipids is shown. During the course of the simulation headgroups are pulled toward charged residues located in the hydrophobic core of the bilayer.

File Name: Supplementary Movie 3

Description: Snapshots from the unrestrained MD simulation of the I1 open morphology in orientation 2 in the bilayer. In this orientation, the PIR and AP domains are in different leaflets of the bilayer. Pink ribbons represent the AP domain, green ribbons the PIR domain. Blue spheres represent the POPC headgroup nitrogen and a surface map of lipids is shown. During the course of the simulation headgroups are pulled toward charged residues located in the hydrophobic core of the bilayer.

File Name: Supplementary Data 1

Description: Code to identify single-molecules and extract the intensity time traces in the photobleaching experiment was done using custom written MATLAB code.

Reporting Summary

Nature Portfolio wishes to improve the reproducibility of the work that we publish. This form provides structure for consistency and transparency in reporting. For further information on Nature Portfolio policies, see our [Editorial Policies](#) and the [Editorial Policy Checklist](#).

Statistics

For all statistical analyses, confirm that the following items are present in the figure legend, table legend, main text, or Methods section.

- | n/a | Confirmed |
|-------------------------------------|--|
| <input type="checkbox"/> | <input checked="" type="checkbox"/> The exact sample size (n) for each experimental group/condition, given as a discrete number and unit of measurement |
| <input type="checkbox"/> | <input checked="" type="checkbox"/> A statement on whether measurements were taken from distinct samples or whether the same sample was measured repeatedly |
| <input type="checkbox"/> | <input checked="" type="checkbox"/> The statistical test(s) used AND whether they are one- or two-sided
<i>Only common tests should be described solely by name; describe more complex techniques in the Methods section.</i> |
| <input checked="" type="checkbox"/> | <input type="checkbox"/> A description of all covariates tested |
| <input checked="" type="checkbox"/> | <input type="checkbox"/> A description of any assumptions or corrections, such as tests of normality and adjustment for multiple comparisons |
| <input type="checkbox"/> | <input checked="" type="checkbox"/> A full description of the statistical parameters including central tendency (e.g. means) or other basic estimates (e.g. regression coefficient) AND variation (e.g. standard deviation) or associated estimates of uncertainty (e.g. confidence intervals) |
| <input type="checkbox"/> | <input checked="" type="checkbox"/> For null hypothesis testing, the test statistic (e.g. F , t , r) with confidence intervals, effect sizes, degrees of freedom and P value noted
<i>Give P values as exact values whenever suitable.</i> |
| <input checked="" type="checkbox"/> | <input type="checkbox"/> For Bayesian analysis, information on the choice of priors and Markov chain Monte Carlo settings |
| <input checked="" type="checkbox"/> | <input type="checkbox"/> For hierarchical and complex designs, identification of the appropriate level for tests and full reporting of outcomes |
| <input checked="" type="checkbox"/> | <input type="checkbox"/> Estimates of effect sizes (e.g. Cohen's d , Pearson's r), indicating how they were calculated |

Our web collection on [statistics for biologists](#) contains articles on many of the points above.

Software and code

Policy information about [availability of computer code](#)

Data collection	NMR Experiments: Bruker Topspin MD simulations: GROMACS 2022 (including implementations of P-LINCS, SETTLE, non-bonded Verlet scheme, PME, velocity-rescale Temperature coupling and Parrinello-Rahman barostat); CHARMM36m protein force field; CHARMM36 lipid parameters; CHARMM-modified TIP3P water model; Super-resolution Fluorescence measurements: ANDOR SOLIS imaging software
Data analysis	NMR experiments, Bruker Topspin (4.0.07), CcpNMR (2.4.2), NMRFAM-Sparky (3.1.9), CYANA (3.98.15) For the analysis of the MD simulation trajectories, the following software and tools were used: GROMACS version 2022 (https://www.gromacs.org/): gmx hbond, gmx mindist; GROMACS version 2022 (https://www.gromacs.org/): gmx hbond, gmx mindist; gmx denisty; gmx gyrate g_contacts (Blau et.al.) used to calculate interatomic distances; Fortran code was used to obtain hydrogen bond energies (Espinosa et. al.) For rendering and plotting, the following software was used: ChimeraX, (1.8) gnuplot 5.4, seaborn, matplotlib and pyplot libraries from Python 3.7. Super-resolution Fluorescence microscopy: DISC algorithm (White et.al.) MATLAB scripts were used to analyze raw image stacks.]. The code to identify single-molecules and extract the intensity time traces in the photobleaching experiment was done using custom written MATLAB code. However, any published codes such as ThunderSTORM can be easily used for the purpose, and available from Ovesny et.al.. The code to fit the intensity time traces is available from White et.al.. The code to fit the binomial distribution of the number of dyes per aggregate was written in MATLAB and provided as a source data file "Binomfit.txt". The code to analyze the polarCOLD data was written by a previous lab

member and described in the following Böning et.al.

For manuscripts utilizing custom algorithms or software that are central to the research but not yet described in published literature, software must be made available to editors and reviewers. We strongly encourage code deposition in a community repository (e.g. GitHub). See the Nature Portfolio [guidelines for submitting code & software](#) for further information.

Data

Policy information about [availability of data](#)

All manuscripts must include a [data availability statement](#). This statement should provide the following information, where applicable:

- Accession codes, unique identifiers, or web links for publicly available datasets
- A description of any restrictions on data availability
- For clinical datasets or third party data, please ensure that the statement adheres to our [policy](#)

Assigned chemical shift data for α S Intermediate 1 were deposited in the BMRB under the accession number 52283. Tables used for structure determination are provided in the Supplement. Source data will be provided with this paper as Source Data. MD simulation data and parameter files are provided through the Edmond data repository at [<https://doi.org/10.17617/3.0V1ODV>]. NMR spectra are deposited at Edmond under [<https://doi.org/10.17617/3.TXND2C>].

Research involving human participants, their data, or biological material

Policy information about studies with [human participants or human data](#). See also policy information about [sex, gender \(identity/presentation\), and sexual orientation](#) and [race, ethnicity and racism](#).

Reporting on sex and gender N/A

Reporting on race, ethnicity, or other socially relevant groupings N/A

Population characteristics N/A

Recruitment N/A

Ethics oversight N/A

Note that full information on the approval of the study protocol must also be provided in the manuscript.

Field-specific reporting

Please select the one below that is the best fit for your research. If you are not sure, read the appropriate sections before making your selection.

☒ Life sciences ☐ Behavioural & social sciences ☐ Ecological, evolutionary & environmental sciences

For a reference copy of the document with all sections, see [nature.com/documents/nr-reporting-summary-flat.pdf](https://www.nature.com/documents/nr-reporting-summary-flat.pdf)

Life sciences study design

All studies must disclose on these points even when the disclosure is negative.

Sample size	NMR experiments: Number of time points in the direct and indirect dimensions were adapted for resolution and signal to noise optimization. Samples tested were transient and multiple samples had to be prepared to obtain assignment spectra and contact spectra. The transient nature of the sample was monitored as described in the Supplement and methods. Once the sample began to change, a new one was prepared for the next measurement. With this methodology, an Intermediate 1 sample was found to be repeatable. Sample sizes and repetitions were determined based on signal to noise ratio required for each spectrum and sample yield. MD simulations: a total of 22 MD simulations of embedded structures were run for 100 ns with distance restraints and an additional 500 ns without restraints to collect data that are evaluated against experimental measurements. For details on sample size and simulation length please refer to MD checklist. Cell experiments were repeated for 6 replicates, often from two separate preparations. Sample size was chosen based on standard practices in the field (i.e. 3 or more biological replicates).
Data exclusions	no data were excluded
Replication	NMR measurements: For each sample prepared, a finger spectrum was obtained that confirmed robust reproducibility of the preparation. MD simulations: in all, for different morphologies and poses, 62 simulations were run. Each condition was run at least in triplicates.
Randomization	no randomization was performed.
Blinding	no blinding was performed

Reporting for specific materials, systems and methods

We require information from authors about some types of materials, experimental systems and methods used in many studies. Here, indicate whether each material, system or method listed is relevant to your study. If you are not sure if a list item applies to your research, read the appropriate section before selecting a response.

Materials & experimental systems

n/a	Involved in the study
<input checked="" type="checkbox"/>	<input type="checkbox"/> Antibodies
<input type="checkbox"/>	<input checked="" type="checkbox"/> Eukaryotic cell lines
<input checked="" type="checkbox"/>	<input type="checkbox"/> Palaeontology and archaeology
<input checked="" type="checkbox"/>	<input type="checkbox"/> Animals and other organisms
<input checked="" type="checkbox"/>	<input type="checkbox"/> Clinical data
<input checked="" type="checkbox"/>	<input type="checkbox"/> Dual use research of concern
<input checked="" type="checkbox"/>	<input type="checkbox"/> Plants

Methods

n/a	Involved in the study
<input checked="" type="checkbox"/>	<input type="checkbox"/> ChIP-seq
<input checked="" type="checkbox"/>	<input type="checkbox"/> Flow cytometry
<input checked="" type="checkbox"/>	<input type="checkbox"/> MRI-based neuroimaging

Eukaryotic cell lines

Policy information about [cell lines and Sex and Gender in Research](#)

Cell line source(s)	SH-SY5Y cells were obtained from ATCC (CRL-2266).
Authentication	SH-SY5Y cells were authenticated by short tandem repeat profiling by ATCC. AT our end, authentication was performed by morphology and replication rate.
Mycoplasma contamination	No mycoplasma was detected in the cultures.
Commonly misidentified lines (See ICLAC register)	No commonly misidentified cell lines were used.

Plants

Seed stocks	N/A
Novel plant genotypes	N/A
Authentication	N/A

Lipidic folding pathway of α -Synuclein via a toxic oligomer

Corresponding Author: Professor Christian Griesinger

This file contains all reviewer reports in order by version, followed by all author rebuttals in order by version.

Version 0:

Reviewer comments:

Reviewer #1

(Remarks to the Author)

The manuscript from Sant and colleagues reported an atomic-resolution structural characterization of a toxic pre-fibrillar aggregation intermediate (I1) on the pathway to forming lipidic fibrils. This structural reconfiguration occurs in a conserved structural kernel shared by many α S-fibril polymorphs, including extracted fibrils from Parkinson's and Lewy Body Dementia patients. Consistent with reports of anti-parallel β -strands being a defining feature of toxic α S pre-fibrillar intermediates, I1 impacts the viability of neuroblasts and disrupts cell membranes, resulting in an increased calcium influx. Our results integrate anti-parallel β -strands as unique features of toxic oligomers with their significant role in the amyloid fibril assembly pathway. These structural insights have implications for the development of therapies and biomarkers.

The study is interesting, with a large panel of new data. However, I have some comments regarding the biological part of their study.

Fig.1C: There is a lack of information regarding the cellular toxicity assays presented. No dose-response or time-response is provided. SHSY5Y is a limited model; other cellular models, such as primary cultures of dopaminergic and/or cortical neurons, would be a good addition, especially with alpha-synuclein.

Line 118: How was the "0.3 μ M α S" concentration determined? Can the authors explain how they measure the concentration/content of alpha-synuclein aggregates? How do they homogenize/normalize the experiment with different alpha-synuclein concentrations?

Fig.S10E and F (i.e., calcium influx experiments). The authors should add information regarding I1 concentration and other experimental conditions.

Fig.4: The authors describe lipids but do not mention which kind of lipids they refer to. Is there a specificity?

Minor comments:

There are references inserted in the abstract

Reviewer #2

(Remarks to the Author)

The manuscript "Lipidic folding pathway of α -Synuclein via a toxic oligomer" by Sant et al describes a structural investigation of oligomeric species of alpha-synuclein (aSyn) that form on the pathway of amyloid fibrils templated on the surface of acidic lipid vesicles. It is of fundamental importance to characterise the nature of intermediates along the self-assembly of aSyn into amyloids as these are considered the toxic species formed in the context of aSyn aggregation, a process that is intimately connected with the insurgence of synucleinopathies such as Parkinson's disease.

In the quest of achieving a high-resolution understanding of the structural properties of a stable oligomeric intermediate (I1), the authors employed a large number of state-of-the art ssNMR experiments as well as super-resolution microscopy, TEM and other biophysical techniques. The study also characterises the toxicity properties of these aggregates when incubated with neuroblastoma cells.

Of particular note is the present finding that antiparallel (AP) regions co-exist with parallel in register (PIR) regions within the same oligomeric assembly of aSyn. This provides a key model to explain how AP-to-PIR transition may occur when toxic intermediates convert into non-toxic mature fibrils. Thus a better understanding of the energy landscape of mature fibrils is now possible. It is likely that initial AP nucleus is formed (with initial intramolecular beta-hairpins forming at the monomeric level and seeding the self-assembly of a small nucleus), followed by the I1 stabilisation through the mixed AP and PIR regions, and in turn the AP-to-PIR transition of the b2 and b3 described in this paper.

Overall, I believe this is a remarkable work that reached an unprecedented level of structural understanding, covering most of the structured part of the aSyn sequence (residues 1-100) within the I1 tetramer. I have few suggestions/curiosities:

- 1) The experimental evidence clearly indicates that I1 has a mixed topology of AP and PIR, by contrast to the fully PIR L2 fibril, and that both PIR and AP are in contact with the lipids, however, it is still not understood why only I1 (i.e. not L2) disrupts the lipids. Previous works (e.g. refs 9, 11) showed from ANS binding that aSyn intermediates are more hydrophobic than the mature fibrils, likely promoting the absorption of the intermediates' cores into the inner hydrophobic region of the lipid bilayer. The present study, by generating ssNMR informed models of I1 could clarify this aspect by detailing (a) if I1 exposes more hydrophobic residues than L2 and (2) if the local conversion AP-to-PIR reduces the exposure of hydrophobic residues as in a typical protein folding process.
- 2) As in previous lipid-bound aSyn intermediate ssNMR analyses, the INEPT regime detected only the C-terminal residues of I1, indicating that the rest of the protein sequence is sufficiently rigid to be probed in CP spectra. Considering the coverage of the resonances in the first 100 residues, it would be very interesting to probe the backbone dynamics, perhaps with transverse relaxation, of the structured regions of the protein. Are the AP regions more dynamical than PIR?
- 3) I'm puzzled by the lack of resonances assigned in the first 15 residues, while it was possible to assign the segment 16-19 and show that this is in alpha-helical conformation. Assuming that the region 1-15 is also alpha-helical, this should be structured as the segment 16-19, possibly leading to detectable sharp lines. Is there an explanation for this lack of resonances (are peaks perhaps too overlapped to be assigned)?

Additional minor points:

- 4) The contact between K96 and residues around A30 in I1 indicated that the scenario might be different in the A30P PD mutation. Does the modelling suggest possible clues on this mutation?
- 5) The manuscript shows many spectra with 1H-15N correlation but I believe that an additional figure with the 13C-13C DARR 20ms of I1 side-by-side to L2 would give a better clue of the properties of the intermediate species compared with the mature fibril.
- 6) Perhaps the text makes an exaggerate use of amyloid-field jargon. For example the "b-arc" is not a general term in structural biology and its structural topology should be described to the general audience. Similarly, in the abstract it is used "lipidic fibrils", which might generate confusion for the audience not familiar with aSyn aggregation on lipid membranes.

Reviewer #3

(Remarks to the Author)

Sant et al. Provide an elegant analysis of the structural transitions of an alpha-synuclein intermediate and the effect this intermediate has on membrane permeability. The authors use ssNMR to characterize the intermediate and distinguish residue-specific interactions of this state from those of the fibrillar structure. Additionally, the authors characterize the stoichiometry of the oligomeric intermediate and utilize experimental constraints to build potential intermediate state models. Finally, the interactions with lipid vesicles were assessed and used to evaluate MD simulations of the modeled intermediate interacting with a lipid bilayer at different orientations. These models suggested a change in membrane permeability that was then validated experimentally to reveal an effect on Ca²⁺ influx induced by the intermediate not induced by preformed fibrils. The authors provide exciting evidence of the formation of hairpin structures distinct from the beta-arch structure in the endpoint fibril states in vitro and reveal an interesting mechanism for a toxic interaction with membranes.

Questions and Comments

- The authors provide models/curve fits of aggregation assays in Figure 1A and Figure S6C without describing the axis or showing the underlying data resulting in the fit presented.
- Comparison of the beta-hairpin to beta-arch transition between I1 and I2 reveals an exciting, energetic barrier that must be overcome to produce the hallmark fibrillar structures associated with the disease. Can this structural transition be observed with directed simulations initiated from the I1 models to a state that satisfies the PIR constraints observed for I2? Detailing this transition and determining if the interactions with the membrane facilitate the change would provide exciting insights into the structural constraints that dictate the kinetics of fibril formation.
- The method of the MD analysis after discarding the initial 750ns or 250ns of the simulation, the lipid contacts were observed using the remaining 250ns. In Supplementary Note 1, this is described differently, as well as in the figure legend of Fig S8, which states only 100ns were used. Consistency in the method description would clarify how the models were developed. Additionally, showing the stability of the secondary structure in the unrestrained simulations would show a correlation with the experimentally observed state.

- In Figure S3, the contact map shows interactions between residues around position 28 and residue 96. However, these constraints seem less satisfied in the MD models of the long constructs (Fig S9C). In orientation 2, the lipid-protein contacts at the N-terminus and position 99 are also less satisfied throughout the replicate simulations (Fig S9A). Orientation 2 contains the states spanning the membrane and showing the lipid bending. Showing how the N and C terminal interactions change over time would illustrate how the penetrance can be driven by the AP domain and not by the termini's more flexible and dynamic interactions.
- The penetrance of Ca²⁺ ions is nicely shown experimentally; however, the Free energy analysis with the addition of Ca²⁺ ions was not described in the methods, details on the simulation length and visualization of intramolecular protein interactions and changes in protein-lipid interactions with the addition of ions would provide a more detailed view of the structural state of I1 as it undergoes this disruptive effect on the membrane.

Overall, the work is clearly described and illustrates an interesting mechanism for the structural transitions in alpha-synuclein assembly. The presented results and supporting evidence would be of broad interest in the field.

Reviewer #4

(Remarks to the Author)

The authors describe in detail a new intermediate aggregate of alpha synuclein that is on pathway to the formation of lipidic fibrils. They use a plethora of experimental techniques to describe in detail the structure of this intermediate structure and how it transitions into a fully formed fibrillar structure.

The manuscript is well written and of interest to the readership.

I only have a few points that need clarification.

1. First, a test was performed for cell viability whereas the authors should have used an Anova to measure significance.
2. The labelling of alpha synuclein was not described in enough detail. Was maleimide labelling used, if yes, please state. Also, how was the labelling ratio determined, in line 513 of the manuscript they state that they used MS (no data shown-please show!), whereas in the supplementary Fig. 4b they say that they measured it using nanodrop, which is highly unprecise, especially if the sample is then used to determine whether the intermediate is a tetramer or not.
3. Related to the above, it is not clear to me how the bleaching experiments are performed with a labelling ratio of 1:4. The same goes for the CODEX assay.
4. Also, the effect of the dye may not have a large effect when one compares NMR spectra of labelled and unlabelled protein, but it has a strong effect on the aggregation dynamics, which has not been addressed in this study.
5. Please provide some brief description of how the CODEX assay works rather than referring to other publications.
6. ThT data shown are highly rudimentary, if included show details of traces and reproducibility by including the standard deviation. Also, in suppl Fig. S1 E is not referred to in the legend.
7. On page 3, line 91-93. "The I1 sample can be isolated for prolonged times in the rotor because it is depleted of disordered monomer and membrane bound monomer (Fig.1A)." Not quite sure what this means. From the context it is supposed to demonstrate how they separated the intermediate from the monomer, but it is not clear how this was done.
8. For Figure 1F, the way the authors labelled the distance between side chains doesn't seem to be following a particular rule (for example from C β - C β from one side chain to the other). Please demonstrate it more clearly.

Version 1:

Reviewer comments:

Reviewer #1

(Remarks to the Author)

All my concerns were satisfactorily addressed by the authors.

Reviewer #2

(Remarks to the Author)

The revised version of the article "Lipidic folding pathway of α -Synuclein via a toxic oligomer" addresses my previous points.

Reviewer #3

(Remarks to the Author)

The authors of Sant. et al. carefully addressed all reviewer comments in the manuscript and improved the rigor of the exciting results presented. The additional MD simulations with the extra analysis and the improved description of the methods improve the interpretation of the atomic detail provided in the models. The authors implemented a range of updates to the simulations that provide a fuller picture of how the transitions observed in the model are driven by interactions

observed in vitro. Additionally, the data interpreting the stability of the truncated I2 oligomer at different sizes and with the lipids shows interesting points to investigate further in other future studies. The authors have presented an improved manuscript with a detailed description of the mechanistic steps transitioning between structural states for alpha-synuclein. This work describes a novel state analysis with supporting experimental and computational models that will be of broad interest in the field.

Reviewer #4

(Remarks to the Author)

I am happy with the refined version of the manuscript

Open Access This Peer Review File is licensed under a Creative Commons Attribution 4.0 International License, which permits use, sharing, adaptation, distribution and reproduction in any medium or format, as long as you give appropriate credit to the original author(s) and the source, provide a link to the Creative Commons license, and indicate if changes were made.

In cases where reviewers are anonymous, credit should be given to 'Anonymous Referee' and the source.

The images or other third party material in this Peer Review File are included in the article's Creative Commons license, unless indicated otherwise in a credit line to the material. If material is not included in the article's Creative Commons license and your intended use is not permitted by statutory regulation or exceeds the permitted use, you will need to obtain permission directly from the copyright holder.

To view a copy of this license, visit <https://creativecommons.org/licenses/by/4.0/>

REVIEWER COMMENTS

Reviewer #1 (Remarks to the Author):

The manuscript from Sant and colleagues reported an atomic-resolution structural characterization of a toxic pre-fibrillar aggregation intermediate (I1) on the pathway to forming lipidic fibrils. This structural reconfiguration occurs in a conserved structural kernel shared by many α S-fibril polymorphs, including extracted fibrils from Parkinson's and Lewy Body Dementia patients. Consistent with reports of anti-parallel β -strands being a defining feature of toxic α S pre-fibrillar intermediates, I1 impacts the viability of neuroblasts and disrupts cell membranes, resulting in an increased calcium influx. Our results integrate anti-parallel β -strands as unique features of toxic oligomers with their significant role in the amyloid fibril assembly pathway. These structural insights have implications for the development of therapies and biomarkers.

The study is interesting, with a large panel of new data. However, I have some comments regarding the biological part of their study.

Fig.1C: There is a lack of information regarding the cellular toxicity assays presented. No dose-response or time-response is provided. SHSY5Y is a limited model; other cellular models, such as primary cultures of dopaminergic and/or cortical neurons, would be a good addition, especially with alpha-synuclein.

Cell viability data for a higher concentration of I1 is included in Fig.1C. At 0.6 μ M α S in I1, the viability decreases compared to 0.3 μ M α S.

For time-response measurements, we refer the reviewer to Fig.4F and Fig.S11. The Calcium influx assay (Fig.4F) and Propidium Iodide fluorescence (PI) (Fig.S11A) are time-resolved measurements. The Calcium influx assay shows that within 15 minutes, the Calcium influx in I1-treated cells exceeds that of control cells, and this difference continues to grow up to 110 minutes. At 110 minutes, the Fluo-4 fluorescence, which increases in response to Calcium concentrations, reaches the maximum achieved by ionomycin (a calcium ionophore), indicating complete disruption of the cell membranes (Fig.4F). Complementarily, the bulk measurement of cell death, observed through the increase in PI fluorescence of the cell-permeable dye (Fig.S11A), shows that cell viability drops around 115 minutes after the addition of I1 and continues to decrease even 24 hours after.

Regarding the use of additional cellular models, we emphasize that the primary focus of this manuscript is structural characterization. The cell viability experiments serve to complement the structural findings with functional assays. SH-SY5Y cells are a well-established model in this context. While we acknowledge the reviewer's suggestion for using primary dopaminergic or cortical neurons, a more detailed biological characterization of I1's effects is beyond the scope of this study. We appreciate the suggestion and will consider it for future research.

Line 118: How was the "0.3 μ M α S" concentration determined? Can the authors explain how they measure the concentration/content of alpha-synuclein aggregates? How do they homogenize/normalize the experiment with different alpha-synuclein concentrations?

We thank the reviewer for pointing out that this was missing in the Methods section. A section called "Determining α S concentration in I1 samples" has been added to the Methods. Briefly, an I1 sample from an ssNMR rotor, once confirmed to have the expected spectrum, was emptied, resuspended in buffer and aliquots were taken for concentration determination.

Aliquots were incubated with 6M Guanidine Hydrochloride (GdHCl) at room temperature for 2-4 hrs to dissociate aggregates. Then the sample was loaded onto a 12% SDS-PAGE gel for densitometric analysis and images of the Coomassie stained gel were obtained on a BIORAD Gel Doc XR with Image Lab software. The intensity of the band at ~15kDa was analyzed with ImageJ to determine the mass of α S loaded and converted to concentrations. To correlate intensity of the band with α S mass, a standard curve was built where the initial α S mass added to the gel was calibrated by measuring absorbance with a 0.2 mm cuvette at 275 nm with an extinction coefficient of $5600 \text{ M}^{-1} \text{ cm}^{-1}$ prior to loading the gel. An attempt was made to measure all I1 samples after GdHCl treatment with absorbance. However, the presence of a high concentration of lipids often lead to baseline distortions specially in the regions around 180 – 300 nm. Note that all concentrations are expressed as monomer equivalents.

Fig.S10E and F (i.e., calcium influx experiments). The authors should add information regarding I1 concentration and other experimental conditions.

The requested information has been added in the new figure Fig.S11.

Fig.4: The authors describe lipids but do not mention which kind of lipids they refer to. Is there a specificity?

A 1:1 mixture of POPC and POPA was the lipid composition for all samples used throughout the study, and the bilayer composition in the simulations. Other lipid compositions were not tested. This information has been added to the legend in Fig4 and in Line 74.

Minor comments:

There are references inserted in the abstract.

These have now been removed.

Reviewer #2 (Remarks to the Author):

The manuscript “Lipidic folding pathway of α -Synuclein via a toxic oligomer” by Sant et al describes a structural investigation of oligomeric species of alpha-synuclein (aSyn) that form on the pathway of amyloid fibrils templated on the surface of acidic lipid vesicles. It is of fundamental importance to characterise the nature of intermediates along the self-assembly of aSyn into amyloids as these are considered the toxic species formed in the context of aSyn aggregation, a process that is intimately connected with the insurgence of synucleinopathies such as Parkinson’s disease.

In the quest of achieving a high-resolution understanding of the structural properties of a stable oligomeric intermediate (I1), the authors employed a large number of state-of-the art ssNMR experiments as well as super-resolution microscopy, TEM and other biophysical techniques. The study also characterises the toxicity properties of these aggregates when incubated with neuroblastoma cells.

Of particular note is the present finding that antiparallel (AP) regions co-exist with parallel in register (PIR) regions within the same oligomeric assembly of aSyn. This provides a key model to explain how AP-to-PIR transition may occur when toxic intermediates convert into non-toxic mature fibrils. Thus a better understanding of the energy landscape of mature fibrils is now possible. It is likely that initial AP nucleus is formed (with initial intramolecular beta-hairpins forming at the monomeric level and seeding the self-assembly of a small nucleus), followed by the I1 stabilisation through the mixed AP and PIR regions, and in turn the AP-to-PIR transition of the b2 and b3 described in this paper.

Overall, I believe this is a remarkable work that reached an unprecedented level of structural understanding, covering most of the structured part of the aSyn sequence (residues 1-100) within the I1 tetramer.

I have few suggestions/curiosities:

1) The experimental evidence clearly indicates that I1 has a mixed topology of AP and PIR, by contrast to the fully PIR L2 fibril, and that both PIR and AP are in contact with the lipids, however, it is still not understood why only I1 (i.e. not L2) disrupts the lipids. Previous works (e.g. refs 9, 11) showed from ANS binding that aSyn intermediates are more hydrophobic than the mature fibrils, likely promoting the absorption of the intermediates' cores into the inner hydrophobic region of the lipid bilayer. The present study, by generating ssNMR informed models of I1 could clarify this aspect by detailing (a) if I1 exposes more hydrophobic residues than L2 and (2) if the local conversion AP-to-PIR reduces the exposure of hydrophobic residues as in a typical protein folding process.

Yes, I1 exposes more hydrophobic residues than the L2-fibril as shown in Fig.S13. The following discussion has been added to the manuscript (lines 382-399):

The I1 surface contains more hydrophobic residues, while in the L2-fibril, these are buried in its fold. Previous work^{3, 28} has shown that α S intermediates are more hydrophobic than fibrils, promoting the absorption of the intermediates exposed hydrophobic surface into the hydrophobic region of lipid bilayers. This is consistent with the I1 structure proposed here. In the absence of lipids, AP β -strands of I1 would have two solvent-exposed interfaces. One interface has a hydrophobic ladder formed by alternating steps of V63 and V55 and the other formed by V66 and V52 (Fig.S13A). In addition, residues A69 and V71 are left exposed due to a wider loop at V74 (Fig.S13A, bottom). Hydrophobic residues in the N- and C-terminal helices, namely V15, V16, A17, A19 A89, A91, I88 and F94 would also be exposed to the solvent (Fig.S13A). The AP to PIR conversion results in the residues V52 and V66 becoming buried in the core of the β -arc formed by two PIR β -strands (Fig.S13B), decreasing the solvent exposed hydrophobic surface. Similarly, the V74 loop gets tighter upon the AP to PIR transition, bringing A69 and V71 closer to A78, and reducing their exposure to the solvent (Fig.S13B). However, the hydrophobic residues I88 and F94 remain exposed to the solvent until the C-terminal strand (β 5) folds onto the β 3 in the L2 fibril, which is after the intermediate 2 stage¹⁷ (Fig.S6D).

2) As in previous lipid-bound aSyn intermediate ssNMR analyses, the INEPT regime detected only the C-terminal residues of I1, indicating that the rest of the protein sequence is sufficiently rigid to be probed in CP spectra. Considering the coverage of the resonances in the first 100 residues, it would be very interesting to probe the backbone dynamics, perhaps with transverse relaxation, of the structured regions of the protein. Are the AP regions more dynamical than PIR?

We thank the reviewer for the interesting suggestion. An (H)NH spectrum can be obtained in a reasonable amount of time, however, only a few resonances are resolved. Therefore, T1 ρ measurements would need to be acquired with an (H)CANH or (H)CONH spectrum, given that a better dispersion of resonances allows us to resolve more peaks. Obtaining a signal to noise ratio of around 30 on an (H)CANH would take 9 days. Thus, multiple 9-day measurements (for each spin lock time) would be needed or around two months to collect enough points to ensure a decay is observed. The limitations on sensitivity and the transient nature of I1, make these measurements extremely challenging but we will keep the suggestion in mind for future work.

3) I'm puzzled by the lack of resonances assigned in the first 15 residues, while it was possible to assign the segment 16-19 and show that this is in alpha-helical conformation. Assuming that the region 1-15 is also alpha-helical, this should be structured as the segment 16-19, possibly leading to detectable sharp lines. Is there an explanation for this lack of resonances (are peaks perhaps too overlapped to be assigned)?

This is indeed curious, and we thank the reviewer for bringing it to our attention. There are two considerations here. First, the affinity of the first ~10 residues of α S for lipid bilayers is dependent on N-terminal acetylation (Maltsev et.al. *Biochemistry* 2012, 51, 25, 5004–5013, Kang et.al. *Protein Science* 2012, 21, 7, 911-917). Previous works have shown that the helical propensity of the first ~10 residues increases upon N-terminal acetylation. In this study, we use nonacetylated α S, suggesting that there may be a smaller population of residues 1-15, than 16-22, that are bound to the lipid membrane and helical.

The second consideration is that residues 10KAKEG14 are one of the many imperfect KTKEGV repeats in the α S sequence. Some of these repeats are part of helices (21KTKQG25) and many are part of loops (32-36, 43-47, 57-61). Chemical shifts in loops appear to show much more dispersion than in helices, suggesting that overlap could indeed be a reason for not observing the first 15 residues. This is also reflected in how only tentative assignments were possible for K23 and Q24 because of overlap in CO resonances and 25GV26 remain unassigned.

Additional minor points:

4) The contact between K96 and residues around A30 in I1 indicated that the scenario might be different in the A30P PD mutation. Does the modelling suggest possible clues on this mutation?

Unfortunately, the I1 structure does not provide any direct clues that might explain the effect of the A30P mutation. There is no reported fibril structure for A30P, and the mechanism for A30P toxicity is generally understood to involve long-lived oligomers (inhibition of fibrils). However, it is not clear how this understanding can be linked to the I1 structure. In the I1 structure, A30 occurs in a loop, buried in the lipid bilayer, connecting the N-terminal helix and PIR β -strands. Proline is generally considered a helix breaker and is frequently found in loops. Given the model, a Proline mutation at this position would not majorly perturb the structure, since the helix is already broken at this position in I1. Furthermore, A30 is followed by G31, which also supports the formation of a loop.

It is entirely conceivable that the A30P mutant drives aggregation toward a different fibril fold than the L2-fibril, implying that the oligomer leading up to such a fibril might be distinct from I1 as well. Since there is no reported fibril structure of an A30P synuclein, it is thus very difficult to predict the effects of the mutation. Even for the L2-fibril A30 is outside the structured region.

5) The manuscript shows many spectra with ^1H - ^{15}N correlation but I believe that an additional figure with the ^{13}C - ^{13}C DARR 20ms of I1 side-by-side to L2 would give a better clue of the properties of the intermediate species compared with the mature fibril.

The ^{13}C - ^{13}C DARR spectra for I1 and the L2-fibril have previously been analyzed in detail in Antonschmidt et.al. *Science Advances* 2021. We have also included the spectra along with assignments in Fig.S1B.

6) Perhaps the text makes an exaggerate use of amyloid-field jargon. For example the “b-arc” is not a general term in structural biology and its structural topology should be described to the general audience. Similarly, in the abstract it is used “lipidic fibrils”, which might generate confusion for the audience not familiar with aSyn aggregation on lipid membranes.

To address this, we have included a schematic to illustrate structural features of a β -arc (Fig.S6A) and lines 247-252. We have also specified what is meant by “lipidic fibrils” in the abstract: “...which incorporate lipid molecules on protofilament surfaces during fibril growth on membranes.”

Reviewer #3 (Remarks to the Author):

Sant et al. Provide an elegant analysis of the structural transitions of an alpha-synuclein intermediate and the effect this intermediate has on membrane permeability. The authors use ssNMR to characterize the intermediate and distinguish residue-specific interactions of this state from those of the fibrillar structure. Additionally, the authors characterize the stoichiometry of the oligomeric intermediate and utilize experimental constraints to build potential intermediate state models. Finally, the interactions with lipid vesicles were assessed and used to evaluate MD simulations of the modeled intermediate interacting with a lipid bilayer at different orientations. These models suggested a change in membrane permeability that was then validated experimentally to reveal an effect on Ca^{2+} influx induced by the intermediate not induced by preformed fibrils. The authors provide exciting evidence of the formation of hairpin structures distinct from the beta-arch structure in the endpoint fibril states in vitro and reveal an interesting mechanism for a toxic interaction with membranes.

Questions and Comments

- The authors provide models/curve fits of aggregation assays in Figure 1A and Figure S6C without describing the axis or showing the underlying data resulting in the fit presented

We would like to point out that Fig1A is just a schematic to illustrate the goals of the study. ThT curves along with fits, raw data and standard deviation from four repeats have been included in Fig.S1E and reproduced in Fig.S6C.

- Comparison of the beta-hairpin to beta-arch transition between I1 and I2 reveals an exciting, energetic barrier that must be overcome to produce the hallmark fibrillar structures associated with the disease. Can this structural transition be observed with directed simulations initiated from the I1 models to a state that satisfies the PIR constraints observed for I2? Detailing this transition and determining if the interactions with the membrane facilitate the change would provide exciting insights into the structural constraints that dictate the kinetics of fibril formation.

The transition from I1 to fibrils occurs via I2 (Antonschmidt *et al. Sci Adv* 7, eabg2174 2021, Fig.S6). While certain aspects are known about I2, like the AP to PIR transition and that the $\beta 5$ is not yet folded, experimentally, we still have many unknowns. For example, is this transition driven by the addition of monomers to I1 or is it just kinetically limited? We are also unclear about the driving force behind the $\beta 5$ folding on $\beta 3$. Efforts to answer these questions are in progress. Unfortunately, ‘brute force’ simulations of the I1 to I2 transition or the de novo assembly from free α Syn monomers is prohibitive due to the long time scales involved in the process, that are not yet accessible even with state-of-the-art MD simulations for the systems in question. Using directed or targeted MD simulations between the two states I1 and I2, however will arguably face the challenge of accurately sampling all relevant configurations of the transition. Running additional MD simulations utilizing truncated models (G36-T81), we have looked at the stability of the L2 fold in the PIR domain and the

AP domain as a function of aggregate size and environment. Indications are that both the successive addition of monomers, as well as the presence of lipid molecules stabilized the L2 fold in I2 oligomers (see **Fig R1**). Although these observations are interesting, they warrant further investigation to carefully examine and separate the exact sequence and specifics of the individual events relevant to the I1 to I2 transition (β -arc folding, loss of lipid contacts in the AP domain, oligomer growth).

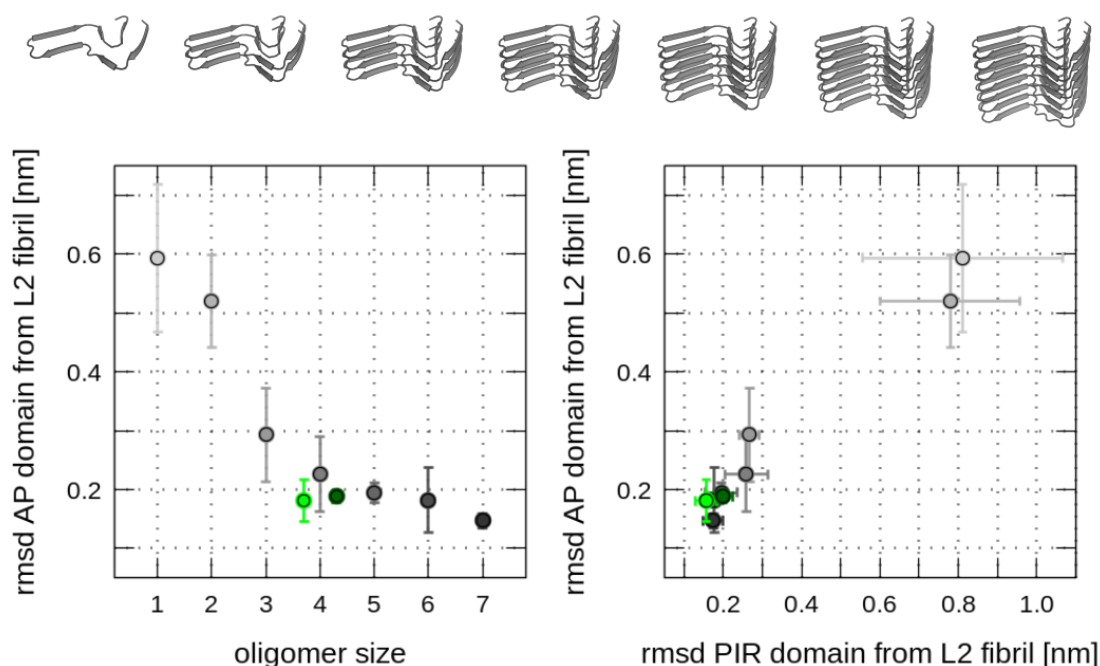


Fig. R1. Size-dependent stability of L2 fold in I2 oligomers. RMSD (Mainchain + C β atoms) for truncated models (G36-T81) of the monomeric L2 fibril conformation as function of aggregate size i.e. number of stacked α S molecules in L2 conformation for residues H50-G67 and the PIR domain (res. 37-44 & 75-80). Circles indicate the average RMSD sampled from the last 50ns of three 250ns long simulations in water and salt without membrane (colors: Monomer – light-gray to Heptamer – dark-gray) and membrane-inserted (Tetramer in Orientation1 – light-green, Tetramer in Orientation 2 – dark-green).

- The method of the MD analysis after discarding the initial 750ns or 250ns of the simulation, the lipid contacts were observed using the remaining 250ns. In Supplementary Note 1, this is described differently, as well as in the figure legend of Fig S8, which states only 100ns were used. Consistency in the method description would clarify how the models were developed. Additionally, showing the stability of the secondary structure in the unrestrained simulations would show a correlation with the experimentally observed state.

We thank the reviewer for pointing out the inconsistency and for giving us the opportunity to clarify the explanation of the simulation analysis. Irrespective of the overall length of the trajectories only the last 250 ns were used throughout all analyses. We corrected the text in the Methods section and Figure captions. We also added Tables S3 and S4 to the Supplementary Material for a more detailed overview of the (length of the) MD simulations. Plots of a secondary structure content analysis were included in a new Fig.S10 in the Supplementary

Material that show a) the stability and the chosen I1 simulation models in terms of secondary structure elements as defined by the DSSP algorithm and b) the high correlation with the experimental assignment.

- In Figure S3, the contact map shows interactions between residues around position 28 and residue 96. However, these constraints seem less satisfied in the MD models of the long constructs (Fig S9C). In orientation 2, the lipid-protein contacts at the N-terminus and position 99 are also less satisfied throughout the replicate simulations (Fig S9A). Orientation 2 contains the states spanning the membrane and showing the lipid bending. Showing how the N and C terminal interactions change over time would illustrate how the penetrance can be driven by the AP domain and not by the termini's more flexible and dynamic interactions.

We would like to clarify that both Orientation 1 and 2 span the membrane and show lipid bending and have a disruptive effect on the membrane (Orientation 1, free energy plot Fig.S10B left, and Orientation 2- right). In the previous simulations, the N- and C- termini are quite far away from each other in the starting coordinates of the MD simulations (see Fig R2, left panels).

The protocol to obtain the atomistic I1 structure models was carried out as follows: Starting from the L2-fibril structure, with the termini taken from micelle-bound α -Synuclein monomer structure, the AP β -strands were formed by imposing distance restraints. These were later removed after equilibration and unrestrained simulations were run. However, no such distance restraints were imposed for the contacts between E28/A30-K96. Instead, this contact was used for validation of the structure and we previously showed that its spontaneous formation is an indication of a model close to experimental contacts. N- and C-terminal interactions were indeed established, however, not in all simulation and only after hundreds of nanoseconds of sampling (see **Fig R2, left panels**).

We undertook a considerable effort to supplement and update the current study with MD simulations that explicitly included the 28/30-96 contacts by initially imposing these distance restraints in the starting models (see Tables S3 and S4). All other aspects of the simulation protocol were left unchanged. As one can see, these new/updated MD simulations do satisfy close N- to C-terminal distances more often in such a set-up (see **Fig R2, right panels**). We used these sets of MD simulations now also for the distance restraints, secondary structure and permeability analysis (see Fig. S10).

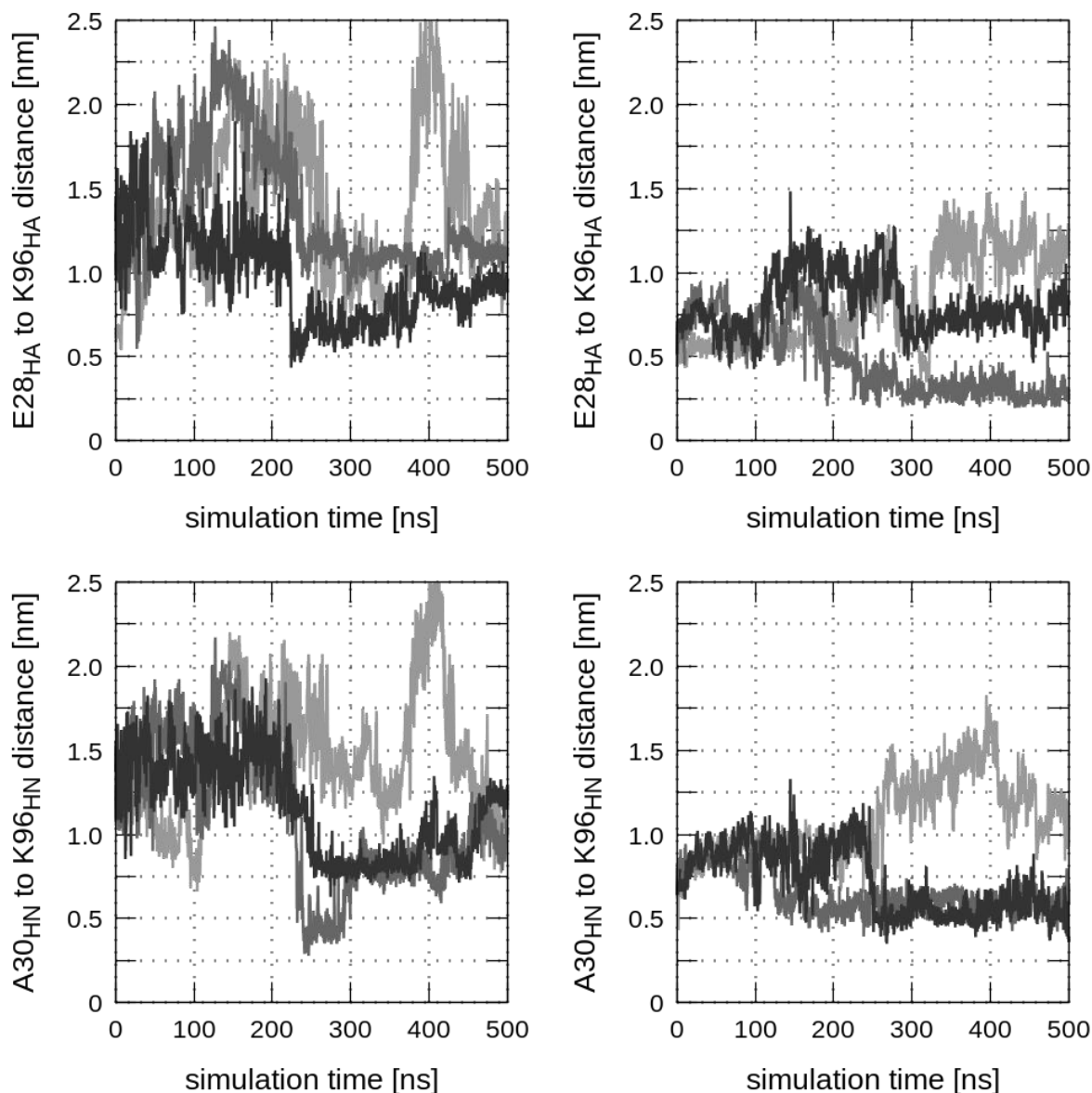


Fig. R2. N- to C-terminal distances in I1 structure models. Exemplary time-course analysis of the HA-HA E28 to K96 and HN-HN A30 to K96 distances for MD simulations of I1 models (open AP morphology; construct: V16-Q99) in Orientation 1 without (left) and with (right) additional structure restraints to improve the N- to C-terminal contacts as observed in experiments.

- The penetrance of Ca^{2+} ions is nicely shown experimentally; however, the Free energy analysis with the addition of Ca^{2+} ions was not described in the methods, details on the simulation length and visualization of intramolecular protein interactions and changes in protein-lipid interactions with the addition of ions would provide a more detailed view of the structural state of I1 as it undergoes this disruptive effect on the membrane.

We thank the Reviewer for pointing this out. We have expanded and streamlined the description of the methods used to analyze the MD simulations. Details of the protein-protein distance restraints, lipid contacts, secondary structure and permeability analysis for the MD simulations with Ca^{2+} ions have been included in a new Fig. S10. We would like to clarify that (permeating)

ions don't alter the structure of the protein or specific, lipid-inserted regions during the simulations. Rather, they are conducted due to the impact of the protein structure on the membrane integrity, i. e. creating polar defects in the hydrophobic bilayer center. As judged from the hundreds of nanoseconds long MD simulations, apart from the initial equilibration of the membrane inserted oligomers no significant changes in protein secondary structure elements specifically in the AP domain were found over time and across all probed simulation systems (see Fig. S10).

Overall, the work is clearly described and illustrates an interesting mechanism for the structural transitions in alpha-synuclein assembly. The presented results and supporting evidence would be of broad interest in the field.

Reviewer #4 (Remarks to the Author):

The authors describe in detail a new intermediate aggregate of alpha synuclein that is on pathway to the formation of lipidic fibrils. They use a plethora of experimental techniques to describe in detail the structure of this intermediate structure and how it transitions into a fully formed fibrillar structure.

The manuscript is well written and of interest to the readership.

I only have a few points that need clarification.

1. First, a test was performed for cell viability whereas the authors should have used an Anova to measure significance.

We thank the reviewer for pointing this out. Statistical analysis has been redone with a one-way ANOVA Tukey test and all significant comparisons are shown in Fig.1C.

2. The labelling of alpha synuclein was not described in enough detail. Was maleimide labelling used, if yes, please state. Also, how was the labelling ratio determined, in line 513 of the manuscript they state that they used MS (no data shown-please show!), whereas in the supplementary Fig. 4b they say that they measured it using nanodrop, which is highly unprecise, especially if the sample is then used to determine whether the intermediate is a tetramer or not.

We would like to bring to the reviewer's attention that mass spectrometry was used at the stage after expression of the protein and binding of the dye to determine if all of the protein is bound to dye in the stock. The requested Mass spectrometry data has been included in Fig.S4B. Subsequently, an aliquot of this dye labeled stock was mixed with dye-unlabeled stock. At this stage, to determine the percentage of dye labeled protein in this mixture, absorbance measurements were used. We would like to highlight that *no nanodrop was used in the study*. Instead, a cuvette of pathlength 0.2 mm was used to load the samples on an HP Agilent spectrophotometer. A section has been included in the Methods called "Absorbance measurements of α S stocks" to outline this.

3. Related to the above, it is not clear to me how the bleaching experiments are performed with a labelling ratio of 1:4. The same goes for the CODEX assay.

We would like to clarify that the CODEX assay is performed with I1 that was prepared with α S containing a single ^{13}C isotopically labeled site at H50 C ϵ . In this case, every molecule in

each aggregate would have an H50 C ϵ that is isotopically labeled and there is no dilution of the label.

On the other hand, photobleaching was performed with I1 prepared with a mixture of wild type α S and A140C α S with ATTO647N at a ratio of 3:1. In this scenario, assuming stochastic mixing, we can expect a distribution of aggregates with varying number of dye-labeled molecules. Some aggregates may contain all dye-labeled molecules, some may have none and other may have intermediate ratios (e.g. 75% or 50% labeled molecules). Each dye molecule photobleaches in discrete steps, and the distribution of the dye labels in aggregates, and the associated probability of observing a certain number of photobleaching steps follows a binomial distribution.

This has been clarified under the section “Oligomer state of I1”, line 191-223.

4. Also, the effect of the dye may not have a large effect when one compares NMR spectra of labelled and unlabelled protein, but it has a strong effect on the aggregation dynamics, which has not been addressed in this study.

We would like to clarify that a mutation and dye tagging, specifically at the A140C position does not affect aggregation kinetics. This is shown in Fig.S4E. We attribute this to the location of the mutation in the disordered domain, far away from the structured portion of I1. We agree with the reviewer that mutations and dye tagging in the structured domain may have an impact on aggregation kinetics and structure. We indeed tried to label the protein in the structured region but the aggregation kinetics and more importantly, the spectra looked different indicating that other structures are formed.

5. Please provide some brief description of how the CODEX assay works rather than referring to other publications.

A more detailed description of the CODEX measurement is provided in lines 195-205.

“An NMR CODEX²¹ (Center band only detection of exchange) measurement allows for spin counting with an upper distance limit of about 10 Å. When each molecule is labeled at a single site, CODEX can be used to determine the oligomer number, provided that the labeled sites form a cluster with the nearest intra-spin distance below 10 Å. For these measurements, I1 was prepared with α S containing a single ¹³C isotopically labeled site at H50 C ϵ . A CODEX measurement involves the decay of initial magnetization of this single isotope labeled nucleus until the signal plateaus at the inverse of the number of spins over which magnetization equilibrates. The CODEX curve reaches about 0.25 at long times, indicating that I1 is at least a 4-mer (Fig.S4A).”

6. ThT data shown are highly rudimentary, if included show details of traces and reproducibility by including the standard deviation. Also, in suppl Fig. SI E is not referred to in the legend.

We thank the reviewer for pointing out this error in the figure legend. An additional panel has been added to Fig.S1 that shows the standard deviation of aggregation kinetics determined by ThT fluorescence as well as the fit, and raw data points to show the aggregation curves of I1 samples used. The kinetics parameters have also been reported in detail in Antonschmidt et.al. Science Advance 2021 (reference 17).

7. On page 3, line 91-93. "The I1 sample can be isolated for prolonged times in the rotor because it is depleted of disordered monomer and membrane bound monomer (Fig.1A)." Not quite sure what this means. From the context it is supposed to demonstrate how they separated the intermediate from the monomer, but it is not clear how this was done.

Thanks for pointing out this confusing/ speculative statement, which has now been improved. The Methods section describes in detail how I1 is separated from monomers by ultracentrifugation. This is also better integrated in the main texts, lines 92-96 of the manuscript:

The I1 sample can be isolated for prolonged times in the rotor (several weeks), which we attribute to a reduction in temperature from 37°C during aggregation to below about 20°C during NMR measurements. Additionally, stability might be improved because I1 has been depleted in disordered monomer and membrane bound monomer via ultracentrifugation before packing.

8. For Figure 1F, the way the authors labelled the distance between side chains doesn't seem to be following a particular rule (for example from C β - C β from one side chain to the other). Please demonstrate it more clearly.

The spectra that were recorded for these measurements ((H)CHH and (H)NHH) allowed for the determination of atom resolved contacts. Therefore, the H α of one residue can be resolved from the H β and so on. The side-chain contacts are labeled according to the resonances observed as explained in lines 151-156. In short, these are atom-resolved contacts.